

**SALT DAMAGE CRITERION PROOF-OF-CONCEPT
RESEARCH TECHNICAL PROGRESS REPORT FOR
THE REPORTING PERIOD FROM OCTOBER 1, 2000,
THROUGH SEPTEMBER 30, 2001**

Topical Report RSI-1557
DE-FC26-00NT41026

prepared for

United States Department of Energy
National Energy Technology Laboratory
626 Cochrans Mill Road
Pittsburgh, Pennsylvania 15236

December 2001



An Integrated Consulting and Services Company

This report was prepared as an account of work sponsored by an agency of the United States Government. Neither the United States Government nor any agency thereof, nor any of their employees, makes any warranty, express or implied, or assumes any legal liability or responsibility for the accuracy, completeness, or usefulness of any information, apparatus, product, or process disclosed, or represents that its use would not infringe privately owned rights. Reference herein to any specific commercial product, process, or service by tradename, trademark, manufacturer, or otherwise does not necessarily constitute or imply its endorsement, recommendation, or favoring by the United States Government or any agency thereof. The views and opinions of authors expressed herein do not necessarily state or reflect those of the United States Government or any agency thereof.

Available to the public from the National Technical Information Service, U.S. Department of Commerce, 5285 Port Royal Road, Springfield, VA 22161; phone orders accepted at (703) 487-4650.

**SALT DAMAGE CRITERION PROOF-OF-CONCEPT
RESEARCH TECHNICAL PROGRESS REPORT FOR THE
REPORTING PERIOD FROM OCTOBER 1, 2000,
THROUGH SEPTEMBER 30, 2001**

Topical Report RSI-1557
DE-FC26-00NT41026

by

Kerry L. DeVries
Kirby D. Mellegard
Gary D. Callahan

RESPEC
P.O. Box 725
Rapid City, South Dakota 57709

prepared for

United States Department of Energy
National Energy Technology Laboratory
626 Cochran's Mill Road
Pittsburgh, Pennsylvania 15236

December 2001

ABSTRACT

This document is the annual technical progress report for Department of Energy Contract No. DE-FC26-00NT41026 entitled *Proof-of-Concept Research for an Advanced Design Criterion to Improve Working Gas Capacity for Natural Gas Storage Caverns in Salt Formations*. This report covers the reporting period from October 1, 2000, through September 30, 2001. During this reporting period, the project was initiated and work was performed to develop structural models that will be used to evaluate two compressed natural gas storage caverns in the McIntosh Dome northwest of Mobile, Alabama. Information necessary to define the structural models include site-specific stress, temperature, geometry, stratigraphy, and operating scenarios in the dome and for the caverns. Additionally, material model development for the salt at the McIntosh Dome was initiated. Material model development activities include acquisition of salt core for testing, laboratory testing, and regression analyses to determine site-specific model parameter values that describe the behavior of salt around a storage cavern. Although not performed during this reporting period, the information and models developed will be used to perform advanced design storage cavern analyses for the Bay Gas caverns to determine the operating pressure ranges to maintain stable conditions.

TABLE OF CONTENTS

EXECUTIVE SUMMARY	1
1.0 INTRODUCTION	3
1.1 BACKGROUND	3
1.2 SCOPE	4
1.3 REPORT ORGANIZATION	5
2.0 SITE CHARACTERIZATION	6
2.1 COMPILATION OF EXISTING DATA	6
2.1.1 Literature Search for Public Domain Records	6
2.1.2 Bay Gas Well No. 1 Existing Data	9
2.2 ACQUIRED DATA FROM THE BAY GAS WELL NO. 2 WELLBORE	13
2.2.1 Bay Gas Well No. 2 Core Retrieval	13
2.2.2 Bay Gas Well No. 2 Wellbore Logging	15
3.0 LABORATORY TESTING	16
3.1 BACKGROUND	16
3.2 TEST SPECIMEN PREPARATION	17
3.3 MECHANICAL PROPERTIES TEST PROCEDURES	17
3.3.1 Brazilian Indirect Tensile Strength Tests	20
3.3.2 Unconfined Compressive Strength Tests	20
3.3.3 Confined Constant Strain Rate Tests	21
3.3.4 Confined Constant Mean Stress Dilation Tests	21
3.3.5 Confined Creep Tests	22
3.4 TEST SYSTEM CALIBRATION PROCEDURES	24
3.5 TEST RESULTS	24
3.5.1 Brazilian Indirect Tensile Tests	25
3.5.2 Unconfined Quasi-Static Compressive Tests	25
3.5.3 Confined Constant Strain Rate Tests	28
3.5.4 Confined Constant Mean Stress Tests	32
3.5.5 Creep Tests	35
4.0 PARAMETER EVALUATION	37
4.1 TECHNICAL APPROACH	37
4.2 NUMERICAL ROUTINES	38
4.3 MODEL FITTING	38
4.4 MDCF RESPONSE MODEL FIT	40

TABLE OF CONTENTS
(Continued)

5.0 DISCREPANCY RESOLUTION AND MODEL REFINEMENT	44
5.1 MDCF MODEL HEALING TERM REFINEMENTS	44
5.2 ALTERNATIVE FORMULATION OF THE POWER-CONJUGATE EQUIVALENT STRESS MEASURES FOR SHEAR-INDUCED DAMAGE	45
6.0 CAVERN ANALYSES.....	46
6.1 BAY GAS WELL NO. 1 MODEL.....	46
6.2 BAY GAS WELL NO. 2 MODEL.....	47
7.0 SUMMARY	49
8.0 REFERENCES	51
APPENDIX A. REVISED MATHEMATICAL FORMULATION OF THE MDCF MODEL HEALING TERM.....	A-1
A.1 DEVELOPMENT OF THE REVISED MDCF MODEL HEALING FORMULATION	A-2
A.2 REDUCTION TO TRIAXIAL COMPRESSION AND TRIAXIAL EXTENSION TESTS.....	A-10
APPENDIX B. POTENTIAL MODIFICATION TO THE POWER-CONJUGATE EQUIVALENT STRESS MEASURES FOR SHEAR-INDUCED DAMAGE	B-1
B.1 REPRESENTATION OF STATES OF STRESS IN PRINCIPAL STRESS SPACE.....	B-3
B.2 ALTERNATE DAMAGE EFFECTIVE STRESS AND FLOW POTENTIAL.....	B-8
B.3 REFERENCES	B-10

LIST OF TABLES

TABLE		PAGE
3-1	Summary of Indirect Tensile Tests.....	25
3-2	Summary of Unconfined Compressive Strength Tests.....	28
3-3	Unconfined Quasi-Static Compressive Elastic Constants	31
3-4	Summary of Confined Constant Strain Rate Strength Tests	31
3-5	Constant Strain Rate Elastic Constants	32
3-6	Summary of CMS Test Results (SI Units).....	33
3-7	Summary of CMS Test Results (English Units)	33
3-8	Creep Test Matrix.....	35
3-9	Steady-State Strain Rate Estimates.....	35
4-1	Functional Groups of MDCF Parameters.....	39

LIST OF FIGURES

FIGURE	PAGE
2-1 Plan View Illustrating the Location of the Bay Gas Caverns at the McIntosh Dome.....	7
2-2 Bay Gas Well No. 1 Cavern Geometry Based on the July 1994 Sonar	10
2-3 Wellhead Pressure of Bay Gas Well No. 1.....	11
2-4 Temperature Profiles From Logs of Bay Gas Well No. 1 From 1994 Through 1998	12
2-5 Illustration of Bay Gas Well No. 2 Cavern Geometry During SMUG Operation.....	14
3-1 Schematic of UTS2 Load Frame and Pressure Vessel	18
3-2 Schematic of Static Creep Test System	19
3-3 $\sqrt{J_2}$ -Versus- I_1 Dilation Criterion	23
3-4 Indirect Tensile Strength as a Function of Depth	26
3-5 Comparison of Tensile Strength of Various Salts.....	27
3-6 Unconfined Compressive Strength as a Function of Depth.....	29
3-7 Comparison of Unconfined Compressive Strength of Various Salts.....	30
3-8 Dilation Criterion Comparison.....	34
4-1 Comparison of Measured and Predicted Creep Tests Performed on Salt From Bay Gas Well No. 2 at 52°C (125°F) and 27.6 MPa (4,000 psi) Confining Pressure	41
4-2 Comparison of Measured and Predicted Stress States for the Onset of Dilation	42
6-1 Two-Dimensional Axisymmetric Finite Element Model of the Bay Gas Well No. 1 Cavern	48
B-1 Illustration of Triaxial Compression and Triaxial Extension Tests Performed on Circular Cylindrical Specimens	B-3
B-2 Stress Points in Principal Stress Space.....	B-5
B-3 Stress Points in Principal Stress Space Viewed Down the Hydrostatic Axis.....	B-5
B-4 Mohr-Coulomb Yield Surface in Principal Stress Space	B-7
B-5 Multimechanism Deformation Coupled Fracture Flow Potential Function Plotted in Principal Stress Space	B-7

EXECUTIVE SUMMARY

This report provides an update of the current status of the Department of Energy (DOE) Contract DE-FC26-00NT41026 as of September 30, 2001. The objective of DOE Contract DE-FC26-00NT41028 is to prove the technology developed for determining the minimum gas pressures of compressed natural gas (CNG) caverns based on the salt damage criterion described by DeVries et al. [1998] and Nieland et al. [1999]. In the earlier work, two major conclusions were reached: (1) the advanced design criterion based on salt damage could be used to reduce the minimum gas pressure in gas storage caverns and (2) an efficient test matrix could be applied to provide site-specific material properties required by the salt constitutive model used for the advanced design criterion. However, these conclusions were based largely on hypothetical information unrelated to a specific application. For example, the cavern analyses related to the first conclusion used the properties for Waste Isolation Pilot Plant (WIPP) damage with the creep characteristics of another salt. This was necessary because WIPP salt is the only salt for which damage parameters have been determined. Through sensitivity studies of simulated test responses, an efficient test matrix was devised that could be used to determine the parameter values for the Multimechanism Deformation Coupled Fracture (MDCF) constitutive model used for the advanced design criterion analyses supporting the second conclusion. However, this test matrix has never been applied to a particular salt formation.

To prove this technology, a proof-of-concept project was formalized by RESPEC and Bay Gas Storage Company, Ltd. (Bay Gas) to refine and demonstrate the use of a new design criterion based on salt damage (microcracking) for determining the minimum gas pressure for storing natural gas in salt caverns. The new design criterion will be applied to two Bay Gas storage caverns (one existing cavern and one newly constructed cavern) in the McIntosh salt dome located northwest of Mobile, Alabama. If successful, the project will have demonstrated that a limited test matrix comprised of approximately 30 tests can be used to define the material model for salt that is capable of predicting the formation and evolution of salt damage that can lead to instability of a salt cavern. Also, the project will demonstrate if working gas capacity for the two Bay Gas caverns can be improved by application of the salt damage criterion.

To meet the objective of this project, the scope of work has been subdivided into six tasks:

1. Site Characterization
2. Laboratory Procedures
3. Parameter Value Determination
4. Model Refinement

5. Cavern Analysis

6. Project Management.

At the time of this report, most of the work has been directed toward developing the “structural and material models” that will be used to evaluate cavern design and operating pressure ranges. Because of the timing of this progress report, complete results for each task are not available and only a general discussion of the work activities performed under this project are provided. A final report will be submitted at the end of this project that will provide considerably more detail and coherence. Below is a brief summary of the status of each task excluding the Project Management task which is not discussed in this report.

Task 1 – *Site Characterization* is essentially complete. All site-specific information necessary to make a geomechanical analysis has been collected as well as salt core for material testing.

Task 2 – *Laboratory Testing* was initiated approximately 2 months behind plan. This delay was due largely to a later-than-anticipated spud date for Bay Gas Well No. 2. The quality of the data obtained to date is considered exceptional; however, testing will likely continue into January 2002.

In an effort to keep the project on schedule, work under Task 3 – *Parameter Evaluation* has been accelerated so that this task will be completed shortly after the laboratory testing task is complete. At the time of this report, 9 of the 24 free parameters of the MDCF model have been determined. The parameters determined describe the isochoric creep (both steady-state and transient) and a preliminary salt dilation boundary. Parameters that describe the evolution of damage, healing, and recovery are yet to be determined.

One of the primary objectives of Task 4 – *Model Refinement* was to update the healing portion of the MDCF model to correct known deficiencies and implement those changes into SPECTROM-32. This objective has been realized; however, planned laboratory testing to evaluate the healing portion of the model has not been undertaken. In addition to updating the healing term, new power-conjugate stress measures for shear-induced damage were formulated. Because most rocks behave differently in triaxial compression and extension with the material being weaker in extension, investigation of new effective stress measures are being pursued.

Other than development of the finite element mesh representation of Bay Gas Well No. 1, little work has been, or can be, done under Task 5 – *Cavern Analysis* until after the parameter evaluation task is complete. According to the project management plan [DeVries, 2001], most of the work to be performed under this task is not scheduled to start until the second quarter of the 2002 government fiscal year (March 2002).

1.0 INTRODUCTION

1.1 BACKGROUND

The working gas capacity of many storage caverns can be increased if the minimum level of internal pressure in storage caverns can be reduced without jeopardizing cavern stability. Geomechanical evaluations are typically used to assess cavern stability during operation. The approach generally used in the geomechanics evaluation of a salt cavern scheduled for compressed natural gas (CNG) storage is to determine an acceptable operating pressure range that meets various design constraints, including the potential for salt dilation [Ratigan et al., 1993]. When the deviatoric stress state (caused by the difference between the gas pressure inside a cavern and the in situ stress of the surrounding salt) becomes too large, dilation (microfracturing resulting in increased porosity) occurs in the salt. Spalling of the salt along the roof or wall of a cavern can occur when the dilation in the salt becomes severe enough to initiate macrofracturing, which may result in loss of containment. RESPEC recently completed a project for the Department of Energy (DOE) which demonstrated that the minimum gas pressure in many CNG storage caverns could potentially be lowered while meeting the design constraints using an advanced design criterion based on the level of damage in the salt [DeVries et al., 1998]. Additionally, the advanced design criterion was deemed economically feasible for use by the CNG industry during the aforementioned project [Nieland et al., 1999].

The objective of the current project is to prove the technology developed for determining the minimum gas pressures of CNG caverns based on the salt damage criterion described by DeVries et al. [1998] and Nieland et al. [1999]. In the earlier work, two major conclusions were reached: (1) the advanced design criterion could be used to reduce the minimum gas pressure in gas storage caverns and (2) an efficient test matrix could be applied to provide site-specific data for the material properties required in the salt constitutive model used for the advanced design criterion. However, these conclusions were based largely on hypothetical information unrelated to a specific application. For example, the cavern analyses related to the first conclusion used the properties for Waste Isolation Pilot Plant (WIPP) damage with the creep characteristics of another salt. This was necessary because WIPP salt is the only salt for which damage parameters have been determined. Through sensitivity studies of simulated test responses, an efficient test matrix was devised that could be used to determine the parameter values for the Multimechanism Deformation Coupled Fracture (MDCF) constitutive model used for the advanced design criterion analyses supporting the second conclusion. However, this test matrix has never been applied to a particular salt formation.

1.2 SCOPE

The scope of work considered in this project represents a proof-of-concept research effort to demonstrate the viability of an advanced design criterion to improve the working gas capacity in natural gas storage caverns. RESPEC, an engineering consulting and services firm, and Bay Gas Storage Company, Ltd. (Bay Gas), a subsidiary of Mobile Gas Service Corporation and a natural gas storage and pipeline company, intend to use the advanced design criterion to design, permit, construct, and operate two Bay Gas storage caverns (one existing cavern and one newly constructed cavern) in the McIntosh salt dome located northwest of Mobile, Alabama. RESPEC and Bay Gas will refine and demonstrate the use of a new design criterion based on salt damage (microcracking) for determining the minimum gas pressure for storing natural gas in salt caverns.

In this research, laboratory tests will be performed to derive accurately and effectively the site-specific creep, damage, and healing parameters of a constitutive model that can be used to assess the stability of compressed natural gas storage caverns. Numerical simulations will be performed using the material properties for salt determined from laboratory testing and the geometrical, operational, and geological model of an existing and a planned storage cavern in the McIntosh Dome. The simulations will be used to establish an operating pressure range for gas storage based on the new design criterion that will result in structurally stable and gas-tight conditions. To meet the objective of this project, the scope of work has been subdivided into six tasks:

1. Site Characterization
2. Laboratory Testing
3. Parameter Value Determination
4. Model Refinement
5. Cavern Analysis
6. Project Management.

The work that was performed during the first year of this contract, under each of these tasks, is discussed in separate chapters of this report, except the Project Management task. The Project Management task was included in this project to provide a separate task for tracking labor hours associated with the preparation and submittal of DOE reporting requirements and general project management activities. Discussion of the project management issues is not warranted for this report.

1.3 REPORT ORGANIZATION

This report contains eight chapters including this introduction. Chapter 2.0 describes the McIntosh site-specific information collected for this study. The laboratory testing program is described in Chapter 3.0. Chapter 4.0 presents preliminary results of the parameter value determination task. The work efforts that have been performed under the Model Refinement Task are given in Chapter 5.0. Chapter 6.0 describes the numerical analyses used to assess cavern stability. Chapter 7.0 provides a brief summary of the progress made during the first year of the project. A list of cited references is given in Chapter 8.0, followed by two appendices containing supporting documentation.

2.0 SITE CHARACTERIZATION

Bay Gas operates a single natural gas storage cavern referred to as Bay Gas Well No. 1 in the McIntosh salt dome located approximately 40 miles northwest of Mobile, Alabama. In addition to the existing cavern, Bay Gas plans to solution mine a 4.22-million-barrel (MMbbls) cavern (Bay Gas Well No. 2) for natural gas storage within the McIntosh Dome. The McIntosh Dome is approximately 1,800 meters (6,000 feet) in diameter with the existing and planned caverns located approximately half-way between the center of the dome and the dome flanks, as shown in Figure 2-1. This chapter describes much of the site information that was gathered and evaluated to determine site-specific information required to perform geomechanical analyses of the existing and planned Bay Gas storage caverns such as: in situ stress, cavern geometry, operating pressure history, and stratigraphy of the surrounding and overlying geologic units. Site characterization activities were divided into categories: (1) compilation of existing material and (2) acquisition of new geologic data from the Bay Gas Well No. 2 wellbore.

2.1 COMPILATION OF EXISTING DATA

Existing data available regarding the operation and local setting at the McIntosh Dome include papers and journal articles in the public domain and records that Bay Gas recorded during the development and operation of Bay Gas Well No. 1. Site-specific information from both of these areas are discussed separately below.

2.1.1 Literature Search for Public Domain Records

In addition to the Bay Gas Well No. 1 natural gas storage cavern, nine brine wells and one compressed air energy storage (CAES) cavern have been developed in the McIntosh Dome. The nine brine wells are operated by Olin Chemical, of which six have been plugged. A literature search was performed to identify relevant public domain publications; most publications discovered were related to the CAES project. Below is a partial list of publications discovered during the literature search. Additional publications on the CAES project can be purchased from the Electrical Power Research Institute (EPRI) but are not given in the following list. Whereas this list is not all inclusive, sufficient information was obtained to proceed with geomechanical analysis without further investigation.

- **Pfeifle, T. W. and J. L. Ratigan, 1993.** *Mechanical Properties Testing and Chemical and Mineralogic Analyses of Salt From the Bay Gas Storage Well #1, McIntosh Dome, Alabama*, RSI-0454, prepared by RE/SPEC Inc., Rapid City, SD, for PB-KBB, Inc., Houston, TX.
- **Mehta, B. R., 1987.** "Status of Compressed Air Energy Storage Project, McIntosh, AL – Part I," *Solution Mining Research Institute Fall Meeting*, Denver, CO, October 19–20.

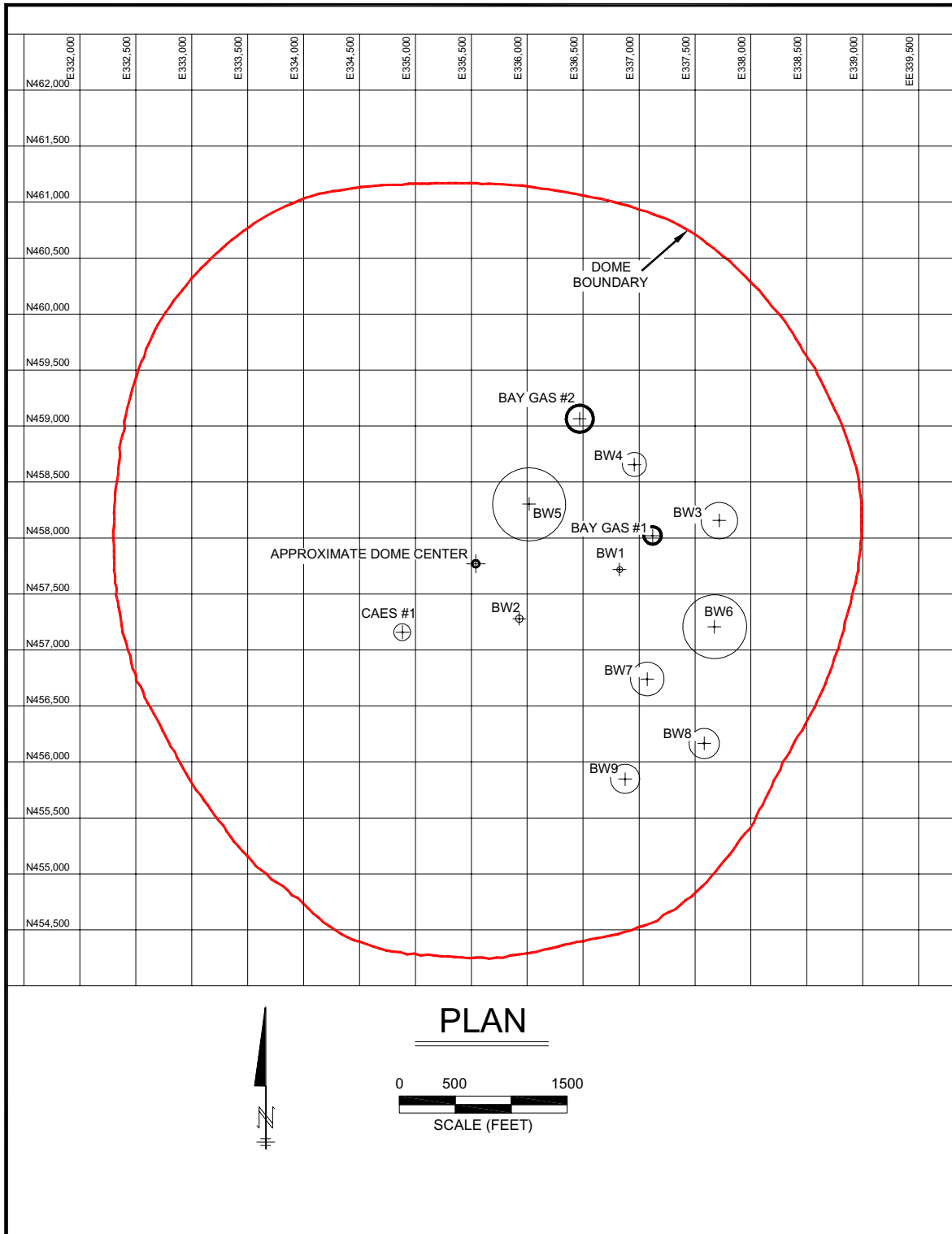


Figure 2-1. Plan View Illustrating the Location of the Bay Gas Caverns at the McIntosh Dome.

- **Medley, A. H., 1987.** “Status of Compressed Air Energy Storage Project, McIntosh, AL – Part II,” *Solution Mining Research Institute Fall Meeting*, Denver, CO, October 19-20.
- **Mehta, B. R., 1988.** “Status of Compressed Air Energy Storage Project, McIntosh, AL – Part I,” *Solution Mining Research Institute Spring Meeting*, Mobile, AL, April 25.
- **Medley, A. H., 1988.** “Status of Compressed Air Energy Storage Project, McIntosh, AL – Part II,” *Solution Mining Research Institute Spring Meeting*, Mobile, AL, April 25.
- **Medley, A. H., 1988.** “Part III – Status of McIntosh, Alabama 100 MW Compressed Air Energy Storage (CAES) Project,” *Solution Mining Research Institute Fall Meeting*, Dallas, TX, October 17–19.
- **Medley, A. H., 1989.** “Status of McIntosh, Alabama 110 MW CAES Project,” *Solution Mining Research Institute Spring Meeting*, New Orleans, LA, May 1.
- **Mehta, B. R., 1987.** “Compressed Air Energy Storage (CAES) in Salt Caverns,” *Solution Mining Research Institute Spring Meeting*, Tulsa, OK, April 27.
- **Thoms, R. L. and R. M. Gehle, 1985.** “Hydrofracture Gradients in Salt Domes – Progress Report,” *Solution Mining Research Institute Fall Meeting*, Houston, TX, October 14–15.
- **Serata, S. and B. Mehta, 1992.** “Design and Stability of Salt Caverns for Compressed Air Energy Storage (CAES),” *Solution Mining Research Institute Spring Meeting*, Kyoto, Japan, April 6–9.
- **Serata, S., B. Mehta, and M. Hiremath, 1989.** “Geomechanical Stability Analysis for CAES Cavern Operation,” *Storage of Gases in Rock Caverns*, Nilsen and Olsen (eds.), A. A. Balkema, Rotterdam, pp. 129–135.
- **Dahlstrom, D. J., 1988.** *McIntosh Dome Salt Core Testing*, Technical Letter Memorandum RSI/TLM-150, prepared by RE/SPEC Inc., Rapid City, SD, for CAES Technology, Palo Alto, CA.

Many of the reports on the CAES project concerned the topic of economics; however, a few of the papers provided a limited discussion on numerical modeling studies and underground construction. Helpful information determined from the literature search included: (1) stratigraphy surrounding the dome, (2) approximate dome geometry, (3) approximate location and dimensions of brine caverns within the dome, and (4) elevation of the brine and CAES caverns. Based on this information, it was assumed that the Bay Gas caverns are sufficiently remote from other caverns and the flanks of the salt dome that they will not influence the numerical analysis results. Therefore, structural models of the Bay Gas storage caverns can assume single isolated caverns developed in an all-salt formation.

2.1.2 Bay Gas Well No. 1 Existing Data

Existing data associated with Bay Gas Well No. 1 and the local setting at the McIntosh salt dome were obtained from Bay Gas and reviewed. Data obtained include:

1. Temperature surveys taken between 1994 and 1998 of Bay Gas Well No. 1
2. Litho density and gamma ray logs of the Bay Gas Well No. 1 wellbore
3. Maps illustrating well locations, cavern spacings, and the salt dome boundary at the McIntosh salt dome
4. Bay Gas Well No. 1 cavern pressure history
5. Sonar data of Bay Gas Well No. 1 taken in 1994 and 2001
6. Casing shoe depth of Bay Gas Well No. 1
7. Sediment and caprock thickness and elevation.

Figure 2-2 illustrates the geometry of Bay Gas Well No. 1 based on the 1994 sonar. Drilling of this cavern began in August 1992 with the cavern put into service about 2 years later (September 1994). The initial solution-mined cavern volume was approximately 2.7 MMbbls. As shown in Figure 2-2, the cavern has a flat roof and a nearly cylindrical shape between depths of 1,265 and 1,494 meters (4,150 and 4,900 feet) with an average diameter of approximately 50 meters (164 feet). Between depths of 1,494 and 1,524 meters (4,900 and 5,000 feet), the cavern diameter tapers to 22 meters (72 feet). The cavern diameter remains essentially unchanged until the bottom of the cavern at a depth of 1,615 meters (5,300 feet).

The casing shoe of the cavern is located at a depth of 1,223 meters (4,012 feet) below ground with the top of salt located at a depth of approximately 121.9 meters (400 feet). Approximately a 6-meter-(20-foot)-thick caprock lies on top of the salt with sediments extending above the caprock to ground surface.

Since the cavern was put into service in 1994, it has been used to supply natural gas to Alabama Electric Cooperative for electrical power generation. Seasonal variations in cavern pressure are the predominant trend with peak pressure in the cavern occurring during the summer months and minimum pressure in the cavern occurring during the winter months, as shown in Figure 2-3. During the last 6 years of service, cavern pressures typically ranged between 21.0 MPa (3,050 psi) and 9.0 MPa (1,300 psi), but has been as low as 8.4 MPa (1,217 psi).

The annual temperature logs taken between 1994 and 1998 from Bay Gas Well No. 1 were examined. Temperature as a function of depth obtained from each of these logs is provided in Figure 2-4. As shown in Figure 2-4, the temperature gradient is essentially linear with depth

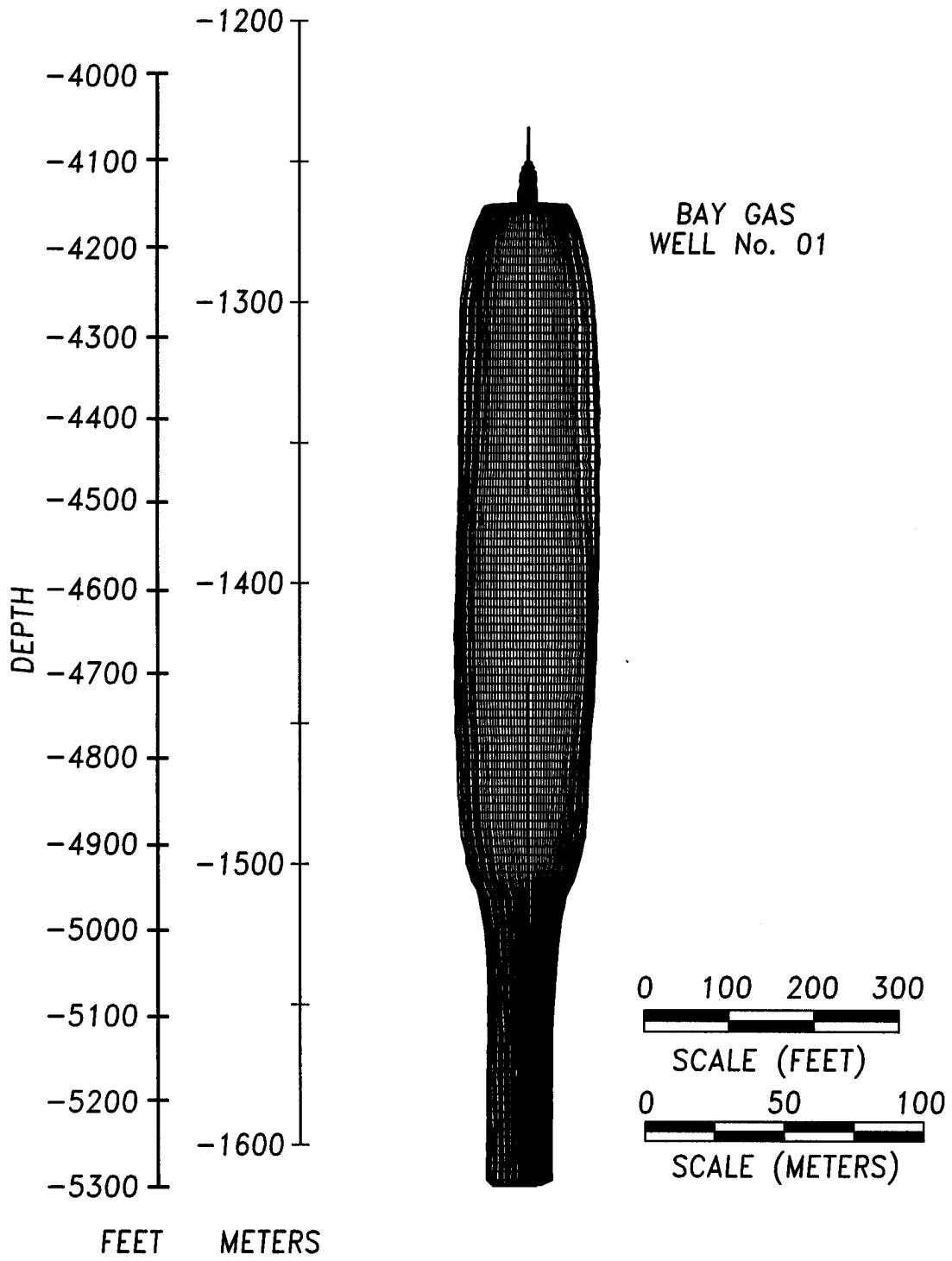


Figure 2-2. Bay Gas Well No. 1 Cavern Geometry Based on the July 1994 Sonar.

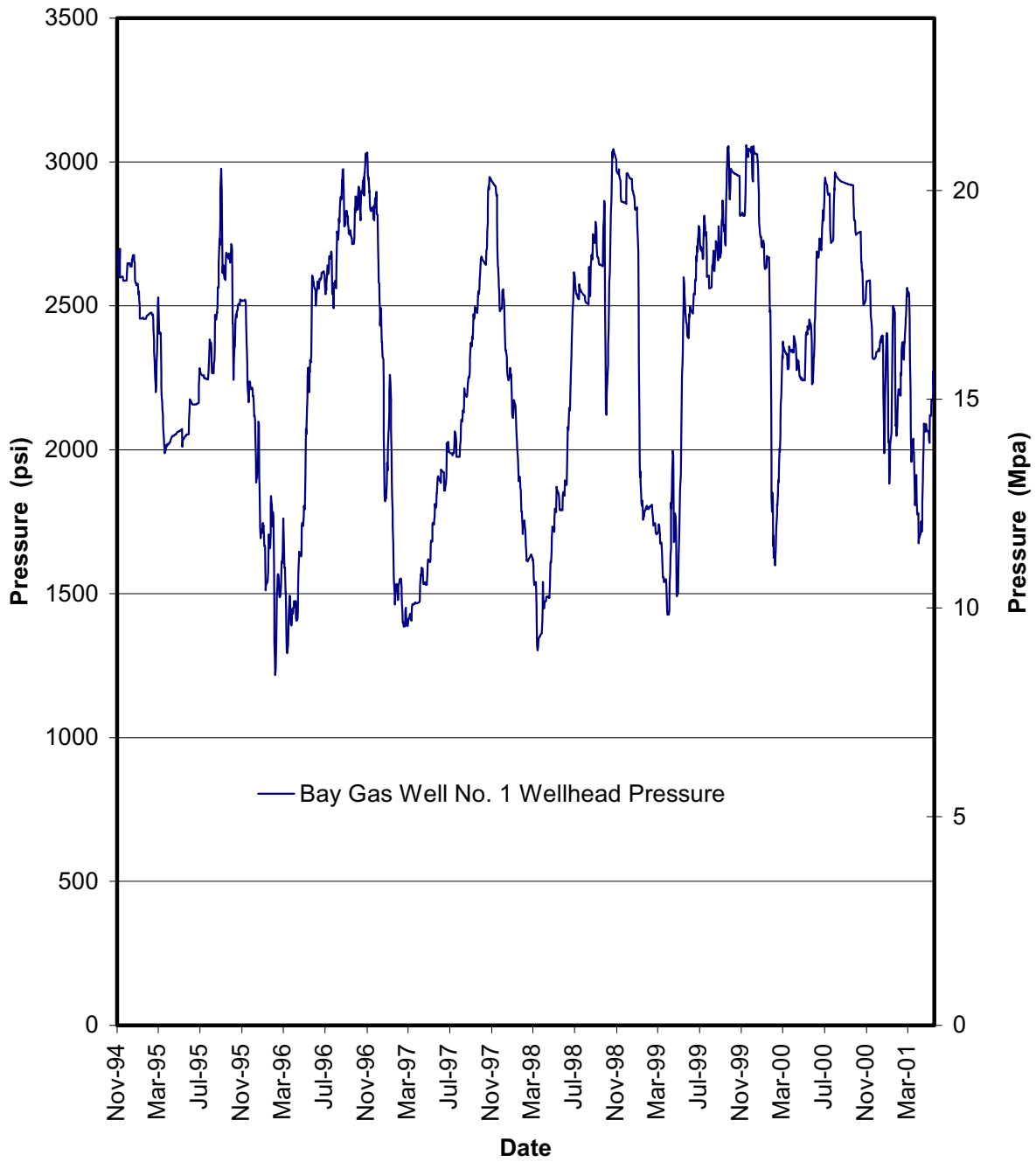


Figure 2-3. Wellhead Pressure of Bay Gas Well No. 1.

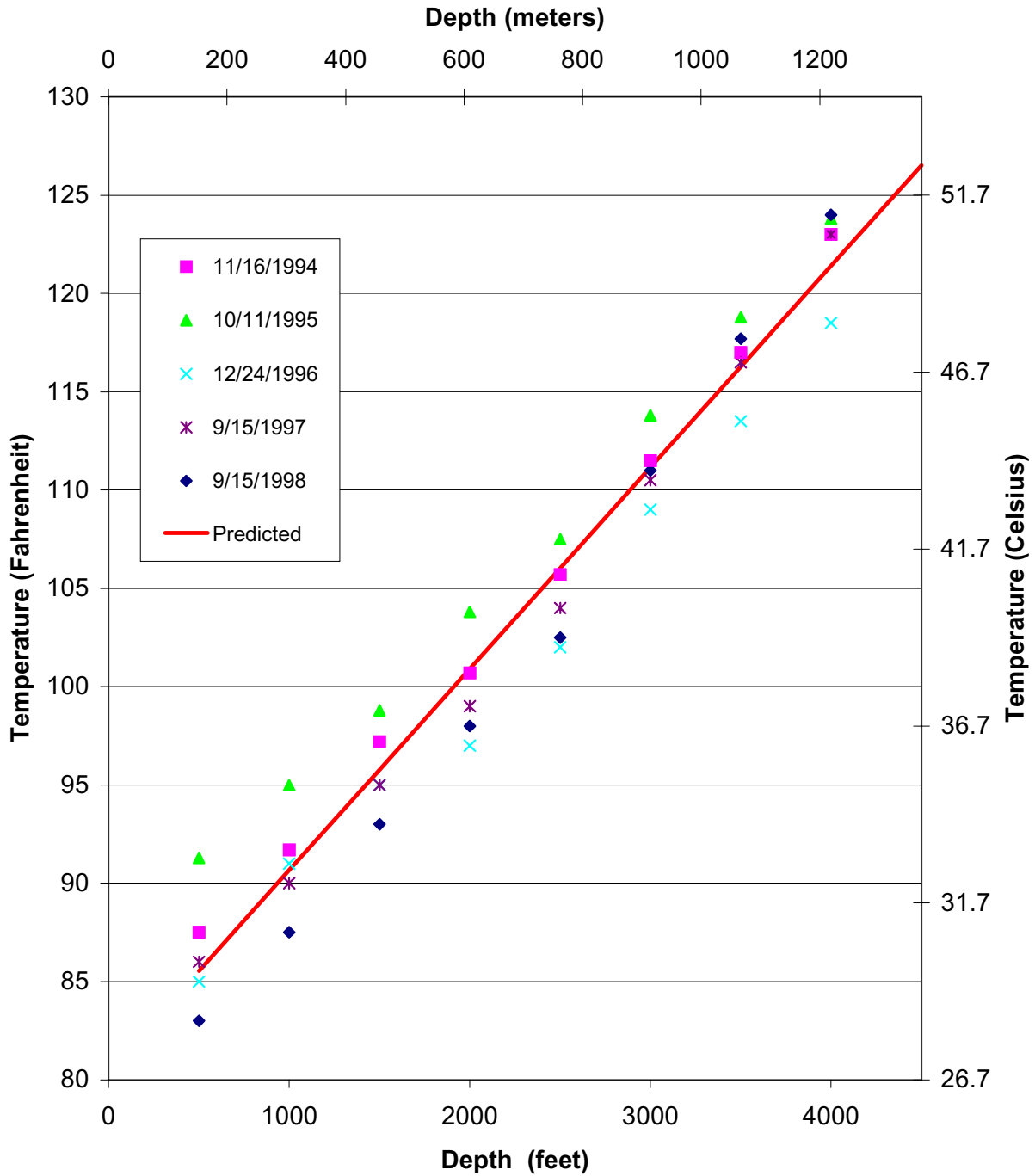


Figure 2-4. Temperature Profiles From Logs of Bay Gas Well No. 1 From 1994 Through 1998.

between elevations of 152 and 1,219 meters (500 and 4,000 feet). Based on this data, a surface temperature of 26.9°C (80.4°F) and geothermal gradient of 0.018675°C/meter (0.01025°F/foot) will be used to define the in situ temperature at the McIntosh Dome.

2.2 ACQUIRED DATA FROM THE BAY GAS WELL NO. 2 WELLBORE

Drilling of the wellbore for the Bay Gas Well No. 2 natural gas storage cavern was initiated on February 7, 2001. Since that time, the wellbore was drilled to a total depth of 1,603 meters (5,260 feet) below ground surface and cased to a depth of 1,246 meters (4,090 feet). Wellbore logging was performed following drilling of the wellbore to final depth. Solution mining of the cavern is currently underway and will take more than 1 year to complete. The final geometry of the cavern based on a solution-mining simulation was provided to RESPEC by Sofregaz US (Sofregaz US is the contractor awarded to design and develop the cavern and has recently been bought by PB-KBB) and is provided in Figure 2-5. It is anticipated that the cavern will be put into operation after 1 year of solutioning; however, solutioning of the lower portion of the cavern will continue under gas until the final cavern volume is obtained. Following solution mining, the maximum diameter of the cavern is expected to be 73.2 meters (240 feet).

2.2.1 Bay Gas Well No. 2 Core Retrieval

A total of approximately 36 meters (120 feet) of rock-salt core was recovered from the Bay Gas Well No. 2 wellbore at locations near the (1) top of the cavern, (2) cavern midheight, and (3) bottom of the cavern. A 9-meter-(30-foot)-long core-barrel was used to cut 100 millimeters diameter (4-inch) salt core. Approximately 18 meters (60 feet) of core were taken from near the top of the cavern between depths of 1,250.0 and 1,267.6 meters (4,101 and 4,158 feet). Nine meters (30 feet) of core were taken from near the cavern midheight between depths of 1,411 and 1,420 meters (4,630 and 4,660 feet). Similarly, 9 meters of core were taken from the bottom of the wellbore at depths between 1,594 and 1,603 meters (5,230 and 5,260 feet). The core samples were wrapped in Saran Wrap to prevent moisture loss and packed in protective tubing to prevent damage before being shipped to the RESPEC Materials Testing Laboratory in Rapid City, South Dakota.

Not all of the recovered core was suitable for testing using the RESPEC rock testing machines. The outer surface of approximately 8 meters (25 feet) of core obtained near the top of the cavern between 1,250 and 1,257 meters (4,101 and 4,126 feet) below ground surface was severely eroded when less than fully salt-saturated drilling mud was used during coring. However, the next 10 meters (33 feet) of core were deemed suitable for testing and provided enough finished test specimens to complete the proposed test matrix described in Chapter 3.0. Salt core recovered from near the midheight and bottom of the cavern was also shipped to RESPEC. This core was used to determine if the mineralogic and mechanical properties of the salt vary with depth and to provide additional salt specimens for testing as needed.

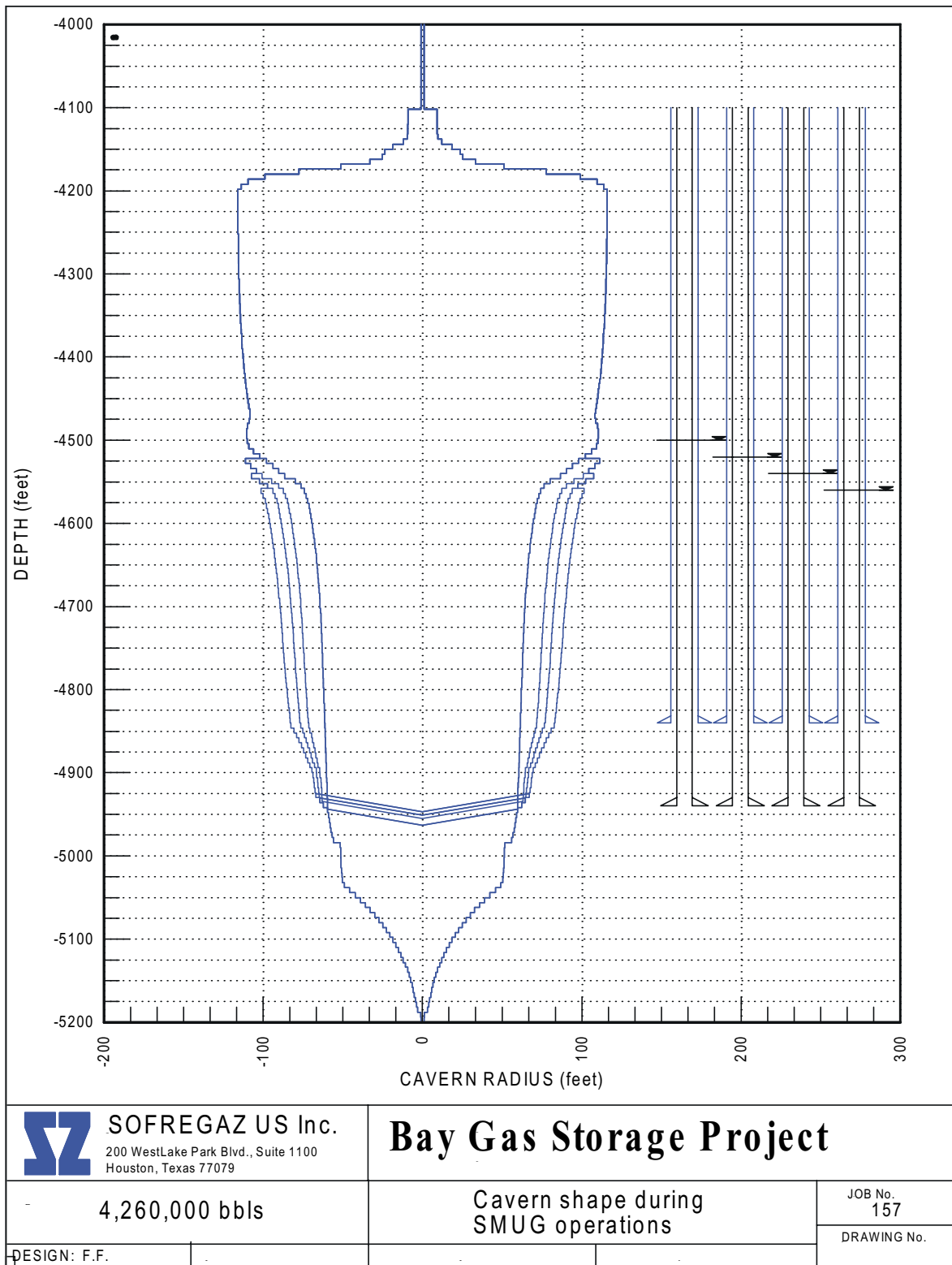


Figure 2-5. Illustration of Bay Gas Well No. 2 Cavern Geometry During SMUG Operation.

2.2.2 Bay Gas Well No. 2 Wellbore Logging

Borehole logging was performed by Schlumberger on April 10, 2001, following completion of the wellbore drilling operation of Bay Gas Well No. 2 cavern. The well logs were reviewed and used to help define the site-specific material properties that are required to perform the geomechanical analyses conducted under Task 5 of this project. The downhole measurements taken by Schlumberger include the following logs:

1. Litho Density – used to determine density of material and material interfaces
2. Compensated Neutron – used to determine porosity
3. Gamma Ray – used to detect formation lithology
4. Dual Laterlog – used to determine porosity and composition of pore fluid
5. Long Spaced Sonic – used to determine dynamic properties of the formation.

No major features were discernable from the wellbore logs in the vicinity of the cavern, indicating that the cavern is located in a homogeneous salt formation. As a result, discrete features are not likely to play a role in cavern performance or stability. Based on the aforementioned logs, a lithostatic in situ stress state (i.e., $\sigma_x = \sigma_y = \sigma_z$) is assumed that varies with depth based on the density of the overlying strata determined from the litho density log.

3.0 LABORATORY TESTING

3.1 BACKGROUND

The objective of the proposed laboratory effort is to complete the laboratory tests recommended by Nieland et al. [1999] on salt core from the McIntosh Dome. Laboratory testing is required to determine the site-specific material properties for the McIntosh salt dome. Specifically, material parameter values need to be determined for the advanced MDCF constitutive model for salt.

Following guidance given by Nieland et al. [1999], an efficient test matrix for this project was proposed that comprised load paths and boundary conditions attainable with the computerized, servocontrolled test systems in the RESPEC rock mechanics laboratory. All tests were performed at a single temperature because of the nearly isothermal nature of the anticipated cavern analyses. In addition, the right-circular, cylindrical specimens being tested were prepared from core samples that have a nominal diameter of 100 millimeters (4 inches). A typical length-to-diameter ratio for specimens used in compression tests is between 2.0 and 2.5.

Five types of tests are being used for estimating the parameters. The types of tests being performed are:

- Brazilian indirect tensile strength (BIT) tests
- Unconfined quasi-static compressive (UCC) strength tests
- Confined constant strain rate (CSR) tests
- Confined constant mean stress (CMS) dilation tests
- Confined creep tests.

All testing was performed on salt cores recovered from Bay Gas Well No. 2 drilled into the McIntosh Dome to a depth from ground surface of 1,603 meters (5,260 feet). RESPEC conducted the tests at its facility in Rapid City, South Dakota. The test matrixes were designed so that all mechanical property tests would be performed on specimens recovered from the appropriate depths to assess the variability in the salt along the height of the proposed cavern.

The Brazilian indirect tensile strength tests were performed to determine apparent tensile strength. Tensile strength can be a useful measure for comparisons between rock types and for comparing variations in rock strength from one location to another. The unconfined compression tests provided data for determining: (1) compressive strength, (2) Young's modulus of elasticity, and (3) Poisson's ratio. These strength and deformation properties are used directly in modeling of underground structures, in comparisons between rock types, and in examining variations in rock properties from one location to another. The constant mean stress dilation

tests provide data used exclusively for determining the stress conditions that produce dilation (volume expansion as a result of microfracturing) in the salt. The creep tests were performed to assess the time-dependent deformation properties of the salt.

3.2 TEST SPECIMEN PREPARATION

Bay Gas Storage provided the core used for the laboratory study. The salt core was recovered from the Bay Gas Well No. 2 in the McIntosh Dome. The cores were sealed in plastic, wrapped in bubble wrap, and placed in plastic core tubes for shipping to RESPEC.

All specimen preparation activities were performed under RESPEC Test Procedure 02 (TP-02), RSI Standard Procedure for *Rock Specimen Preparation, Rev 4*. All of the specimens were given a unique identification number for tracking within the RESPEC laboratory. A typical specimen identification number is:

MD/BG2/4145.8

where:

MD = McIntosh Dome

BG2 = Bay Gas Well No. 2

4145.8 = Core recovery depth (feet).

Salt specimens for testing were prepared by initially sawing a specimen from the 100-millimeter-(4-inch-) diameter field core and then finishing the ends with a milling machine. The diameter of the salt specimens was not reduced from that obtained in the field. Final specimen dimensions for the triaxial compression tests were approximately 100 millimeters (4 inches) in diameter and 200 millimeters (8 inches) in length. Final specimen dimensions for the indirect tensile (Brazilian) tests were diameters of 100 millimeters (4 inches) and lengths of 50 millimeters (2 inches).

3.3 MECHANICAL PROPERTIES TEST PROCEDURES

RESPEC personnel performed all the mechanical properties testing of the Bay Gas salt specimens using the laboratory facility located in Rapid City, South Dakota. The strength tests and the dilation tests were performed on a servohydraulic test system shown in Figure 3-1 where the prominent test system components are labeled. One notable feature of the test system shown in Figure 3-1 is the capability to mount the strain-measuring instrumentation directly on the specimen. The creep tests were performed on computerized static loading test systems designed for maintaining stable loads over long periods of time. A typical static load frame is shown in Figure 3-2. A brief description of each type of mechanical properties test is given in separate sections that follow.

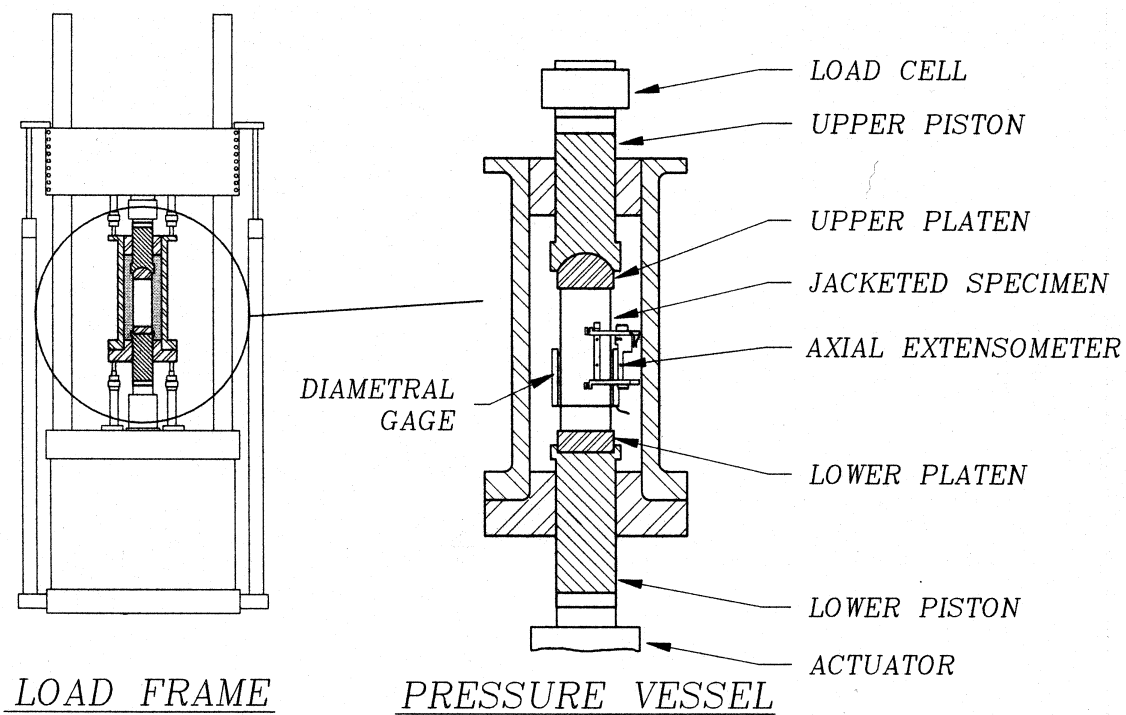


Figure 3-1. Schematic of UTS2 Load Frame and Pressure Vessel.

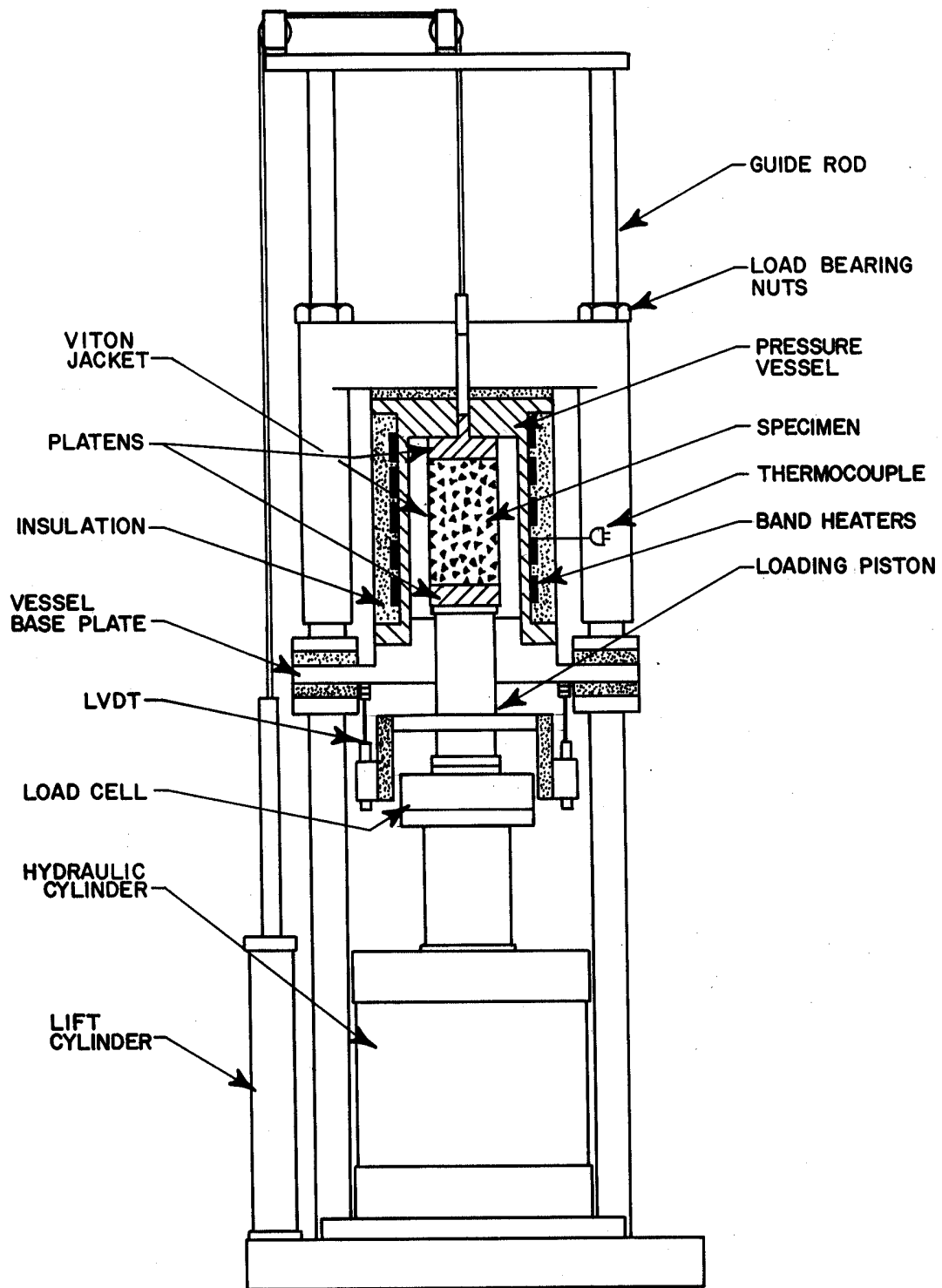


Figure 3-2. Schematic of Static Creep Test System.

3.3.1 Brazilian Indirect Tensile Strength Tests

Apparent tensile strength of the salt was determined by means of the Brazilian indirect tensile (BIT) test. This method is termed an indirect method because a compressive, diametral line load is applied over the length of a cylindrical specimen having a L:D = 0.5:1. The compressive load induces a tensile stress at the center of the specimen perpendicular to the diametral line load. As the compressive line load increases, so does the tensile stress. The tensile strength is computed according to:

$$T_0 = \frac{2P}{\pi DL} \quad (3-1)$$

where:

T_0 = apparent tensile strength, MPa (psi)

P = line load at failure, MN (lbs.)

D = specimen diameter, m (in.)

L = specimen length, m (in.).

3.3.2 Unconfined Compressive Strength Tests

These tests were performed to determine: (1) unconfined compressive strength (UCC) and (2) elastic moduli. The unconfined compressive strength tests were conducted at a temperature of 20°C (68°F) in axial strain control at an axial strain rate of $1 \times 10^{-4} \text{ s}^{-1}$. Unload/reload cycles were conducted on some the specimens. The data collected during these unload/reload cycles were used to estimate the elastic constants; i.e., Young's modulus, E , and Poisson's ratio, ν .

A typical stress-strain curve for an unconfined compression test would show that the stress-strain response during loading is quite nonlinear, particularly at higher stress levels. Initially, the stress increases rapidly with strain; however, the stress eventually reaches a peak and then decreases as the specimen continues to strain. This peak stress is defined as the unconfined compressive strength.

The load path may include an unload/reload cycle characterized by a decrease in stress followed by a comparable increase in stress at an axial strain level of approximately 0.25 to 0.50 percent. The data acquired during the cycle are used to calculate two elastic constants, Young's modulus, E , and Poisson's ratio, ν , using two mathematical equations as follows:

$$E = \frac{\Delta\sigma}{\Delta\varepsilon_1} \quad (3-2)$$

$$v = \frac{E}{\frac{\Delta\sigma}{\Delta\varepsilon_3}} \quad (3-3)$$

where $\Delta\sigma$ is the change in stress and $\Delta\varepsilon_1$ and $\Delta\varepsilon_3$ are the changes in axial and radial strain, respectively. Equation 3-2 and the denominator of Equation 3-3 represent the slopes of the stress versus axial strain and stress versus radial strain curves, respectively, generated during the unload/reload portion of the load path.

3.3.3 Confined Constant Strain Rate Tests

In the confined constant strain rate (CSR) tests, the axial stress, σ_1 , is increased and the confining pressure, σ_3 , is held constant. The primary objective of these tests was to determine the elastic and strength characteristics of the salt.

In the CSR test, the test specimen is first loaded hydrostatically by applying radial stress (or confining pressure), σ_3 , and axial stress, σ_1 , in equal increments until the mean stress specified for the test has been reached. Then a stress difference (difference between the axial stress and the radial stress) is applied by increasing the axial stress while holding the radial stress constant. The application of the stress difference is controlled to maintain a constant axial strain rate. Tests are terminated when the specimen fails.

The stress difference versus strain curves for a typical CSR test are similar to those described for the UCC tests because the UCC test is simply a special case of the CSR test; i.e., a UCC test is a CSR test at a confining pressure of zero. Unload/reload cycles are used in the CSR tests to estimate elastic constants in the same fashion previously described for UCC tests.

3.3.4 Confined Constant Mean Stress Dilation Tests

In the confined constant mean stress (CMS) tests, the axial stress, σ_1 , is increased and the confining pressure, σ_3 , is simultaneously decreased at rates which produce no change in the mean stress ($\sigma_m = (\sigma_1 + 2\sigma_3)/3$) imposed on the specimen. The primary objective of these tests was to determine the dilatational characteristics (volume expansion caused by microfracturing) of the salt.

In the CMS test described by Mellegard and Pfeifle [1998], the test specimen is first loaded hydrostatically by applying radial stress (or confining pressure), σ_3 , and axial stress, σ_1 , in equal increments until the mean stress specified for the test has been reached. Then a stress difference (difference between the axial stress and the radial stress) is applied by increasing the axial stress and simultaneously decreasing the radial stress. During this application of stress difference, the axial stress rate is twice the radial stress rate (with opposite algebraic sign) to maintain a state of constant mean stress. Tests are terminated either when the specimen fails

or when the confining pressure has been completely removed (i.e., tensile radial stresses cannot be induced in the test specimen with this test configuration).

Because the mean stress is not changing during the CMS tests, the volumetric strain remains virtually unchanged or indicates a small level of compaction at low to moderate stress differences. This behavior is consistent with a material that is not dilating. However, at some elevated stress difference, the volumetric strain rate accelerates and the volumetric strain becomes negative,¹ which implies that the specimen is being damaged through microfracturing (creation of voids). The specimen can sustain even larger stress differences beyond the point where dilation begins; however, it also experiences higher levels of damage (dilatant volumetric strain) at these stress conditions.

The data obtained from the CMS tests can be used to develop a relationship between mean stress and the stress difference that produces salt dilation. A common method used to develop such a relationship is to: (1) redefine the mean stress and stress difference levels which induce dilation in terms of stress invariants, and then (2) develop a mathematical model which relates the stress invariants in a manner consistent with the experimental data. Two stress invariants typically used to develop these models are the first invariant of the Cauchy stress tensor, I_1 , and the second invariant of the deviatoric stress tensor, J_2 . When CMS triaxial compression data are available, the two stress invariants can be defined as follows:

$$I_1 = 3\sigma_m = \sigma_1 + 2\sigma_3 \quad (3-4)$$

$$\sqrt{J_2} = \frac{\Delta\sigma}{\sqrt{3}} = \frac{\sigma_1 - \sigma_3}{\sqrt{3}} \quad (3-5)$$

The data can be plotted in the $\sqrt{J_2}$ -versus- I_1 stress space, as shown in Figure 3-3, where the data will generally follow a more or less linear trend in this stress space. A line fitted to the data will divide the stress space shown in Figure 3-3 into two distinct regions. The region above and to the left of the line represents stress states where dilation will occur, while the region below and to the right of the line represents stresses where dilation will not occur. This dilation limit can be used directly in geomechanical analysis of underground caverns to determine regions in the salt that may be susceptible to dilation.

3.3.5 Confined Creep Tests

Confined creep tests are performed to evaluate the time-dependent behavior of materials (e.g., salt). A creep test is initiated by applying confining pressure to all exterior surfaces of a specimen that has been jacketed in a flexible membrane to protect it from the pressurizing medium and then heating the jacketed specimen to the prescribed test temperature. Once the

¹ Compressive stresses and strains are signed positive so negative volumetric strains imply a volume expansion.

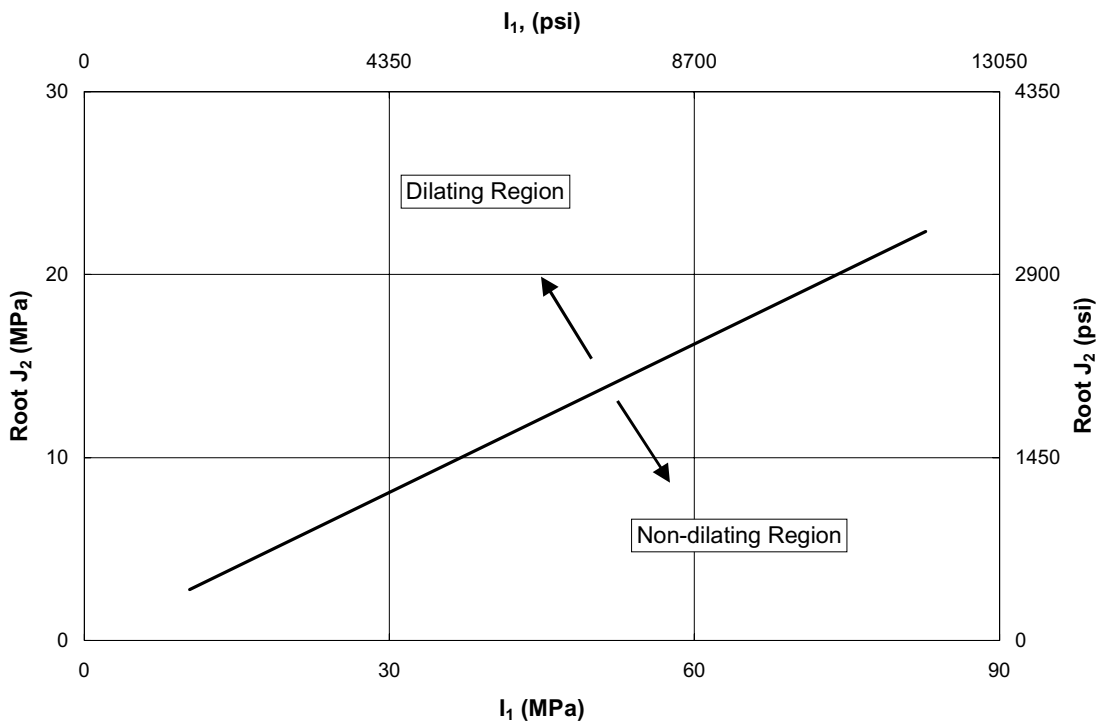


Figure 3-3. $\sqrt{J_2}$ -Versus- I_1 Dilation Criterion.

confining pressure and temperature are stable, axial stress is quickly applied to the ends of the specimen until the target stress difference is reached, at which time, the confining pressure and stress difference are maintained at their specified levels for the duration of the test or until a subsequent stage is initiated by changing the level of applied axial stress.

During the test, axial force, confining pressure, axial displacement, radial displacement, and temperature are recorded. Axial stress is calculated from the axial force and the current cross-sectional area of the specimen. Axial and radial true (logarithmic) strains are calculated from the axial and radial displacements and the specimen dimensions. A typical strain versus time response from a creep test would show that at early times, the strain rates are high immediately after the increase in axial stress but then decrease with time as they approach nearly constant values.

3.4 TEST SYSTEM CALIBRATION PROCEDURES

The testing requires use of sophisticated, computer-controlled test systems equipped with electronic transducers used to measure force, pressure, displacement, and temperature. The transducers are calibrated at regular intervals using certified in-house standards that are traceable to the National Institute of Standards and Technology (NIST).

Verification procedures indicate that the transducer readings are accurate within 1 percent for load and pressure measurements and 2 percent for deformation and volume measurements. Also, temperature measurements are accurate within 2°C. The testing systems, including the electronics, are housed in an environmentally controlled facility in which the temperature is maintained at $20 \pm 1^\circ\text{C}$ ($68 \pm 2^\circ\text{F}$).

3.5 TEST RESULTS

Five types of mechanical properties tests were performed on the salt core recovered from Bay Gas Well No. 2, including:

- Brazilian indirect tensile (BIT) strength tests
- Unconfined quasi-static compressive (UCC) strength tests
- Confined constant strain rate (CSR) strength tests
- Confined constant mean stress (CMS) dilation tests
- Confined creep tests.

The mechanical results of the tests are presented separately in the sections that follow.

3.5.1 Brazilian Indirect Tensile Tests

Six indirect tensile tests were performed. Two tests were performed on salt recovered from each of three nominal depths, 1,263 meters (4,145 feet), 1,416 meters (4,646 feet), and 1,595 meters (5,232 feet). All tests were performed at a temperature of 20°C (68°F). The test results are summarized in Table 3-1. The tensile strengths ranged from a low of 1.11 MPa (161 psi) to a high of 1.54 MPa (223 psi) and averaged 1.38 MPa (200 psi).

Table 3-1. Summary of Indirect Tensile Tests

Specimen I.D.	Depth		Strength	
	(m)	(ft)	(MPa)	(psi)
MD/BG2/4145.2	1,263	4,145.2	1.527	221.4
MD/BG2/4145.4	1,264	4,145.4	1.392	201.9
MD/BG2/4646.5	1,416	4,646.5	1.108	160.7
MD/BG2/4646.7	1,416	4,646.7	1.539	223.2
MD/BG2/5232.2	1,595	5,232.2	1.303	189.0
MD/BG2/5232.4	1,595	5,232.4	1.410	204.5

The tensile strengths given in Table 3-1 are plotted as a function of depth in Figure 3-4. The figure indicates that the tensile strength does not vary greatly among the three depths investigated, although the salt near the roof of the proposed cavern has the highest average strength. The tensile strengths in Table 3-1 are also compared with tensile strengths observed for several other salt types [Pfeifle et al., 1995] in Figure 3-5. The figure shows the average strength of each salt type along with error bars that indicate the range of values that were reported. The figure shows the tensile strength is similar to the tensile strengths determined for other salts.

3.5.2 Unconfined Quasi-Static Compressive Tests

Six unconfined quasi-static compressive tests were performed. Two tests were performed on salt recovered from each of three nominal depths of 1,265 meters (4,150 feet), 1,414 meters (4,637 feet), and 1,595 meters (5,233 feet). The compressive strength tests were conducted at a temperature of 20°C (68°F) in axial strain control at an axial strain rate of $1 \times 10^{-4} \text{ s}^{-1}$.

Table 3-2 provides a summary of the unconfined compressive strengths determined from the six tests. The unconfined compressive strengths ranged from a low of 15.3 MPa (2,219 psi) to a high of 18.3 MPa (2,659 psi) and averaged 17.1 MPa (2,477 psi).

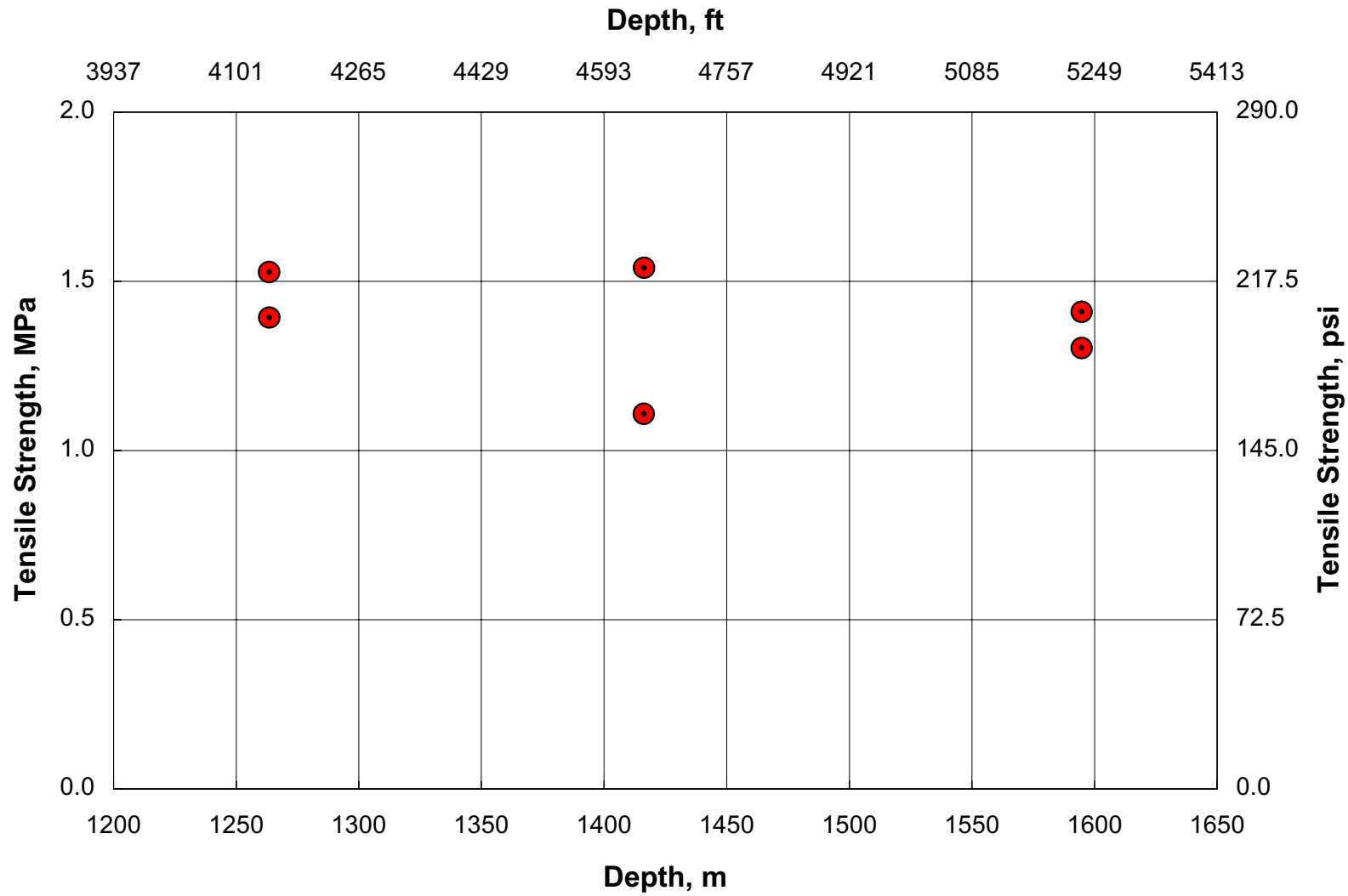


Figure 3-4. Indirect Tensile Strength as a Function of Depth.

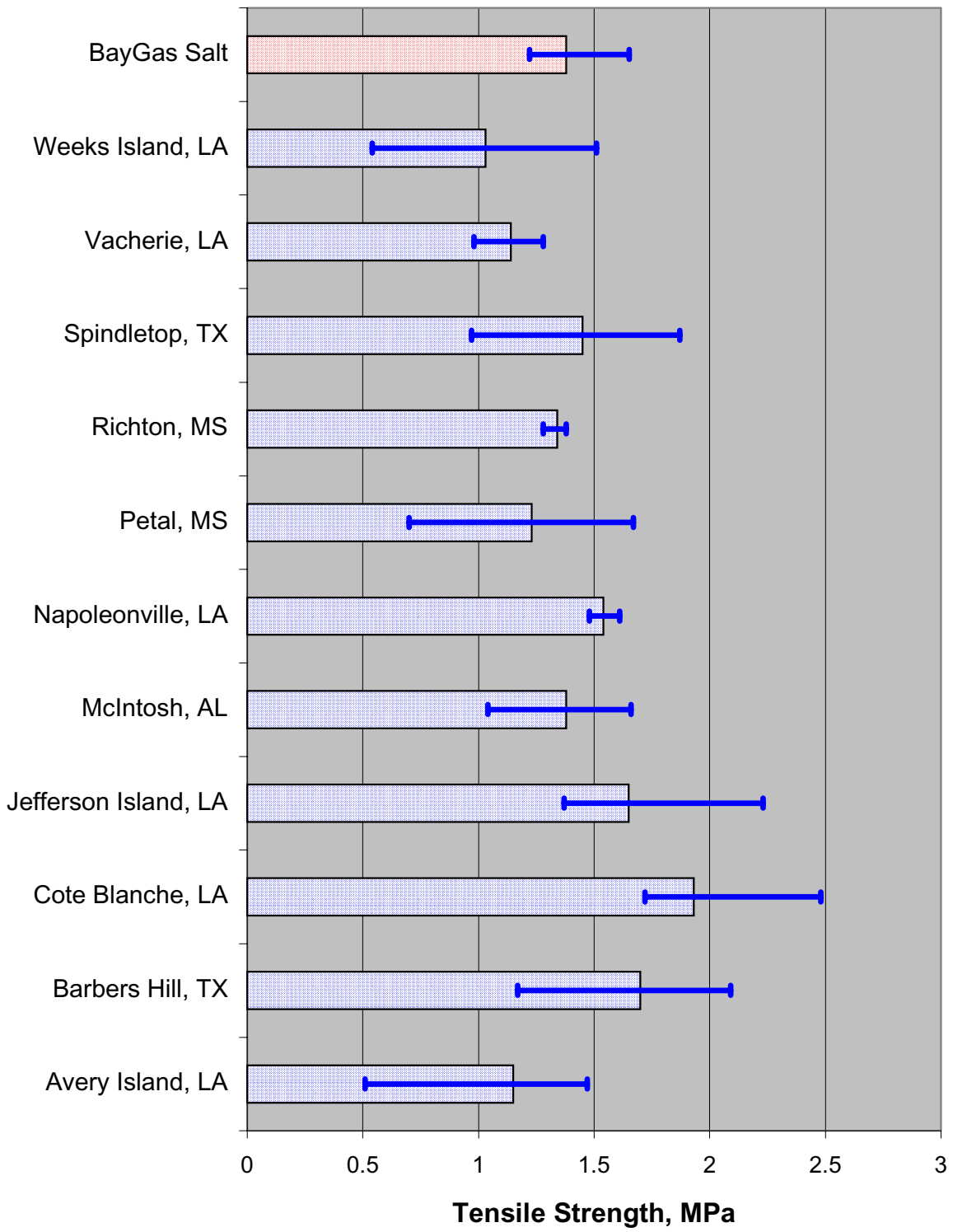


Figure 3-5. Comparison of Tensile Strength of Various Salts.

Table 3-2. Summary of Unconfined Compressive Strength Tests

Specimen I.D.	Depth		Strength	
	(m)	(ft)	(MPa)	(psi)
MD/BG2/4149.8	1,265	4,149.8	16.1	2,333
MD/BG2/4153.0	1,266	4,153.0	15.3	2,219
MD/BG2/4637.1	1,413	4,637.1	17.8	2,575
MD/BG2/4637.7	1,414	4,637.7	17.3	2,503
MD/BG2/5232.9	1,595	5,232.9	17.7	2,572
MD/BG2/5233.6	1,595	5,233.6	18.3	2,659

The unconfined compressive strengths given in Table 3-2 are plotted as a function of depth in Figure 3-6. The figure indicates that the unconfined compressive strength is lowest at the depth corresponding to the roof of the proposed cavern and increases with depth. The strengths in Table 3-2 are also compared with unconfined compressive strengths observed for several other salt types [Pfeifle et al., 1995] in Figure 3-7. The figure shows the unconfined compressive strength is similar to the strengths determined for other salts.

All of the specimens in Table 3-2 incorporated unload/reload cycles in their load paths to generate data for estimating values of Young's modulus and Poisson's ratio. The elastic constants obtained from the tests are given in Table 3-3. The average value of Young's modulus was 19.6 GPa (2,835,504 psi) with no apparent trend between Young's modulus and depth. The values for Poisson's ratio given in Table 3-3 are generally larger than the value of about 0.35 that would be expected for salt. In fact, three of the specimens displayed values greater than 0.5, which is a value expected for an incompressible material. The explanation for this variance lies in the large crystal sizes seen in the salt. A general rule in testing cylindrical specimens of salt is that the specimen diameter should contain at least ten individual crystals. In many cases, these salt specimens had less than ten crystals through a diameter and the action of a few large crystals yielded unrepresentative radial deformations.

3.5.3 Confined Constant Strain Rate Tests

Six confined constant strain rate tests were performed. Two tests were performed on salt recovered from a nominal depth of 1,260 meters (4,134 feet) at each of three constant confining pressures: 1.0 MPa (150 psi), 5.2 MPa (750 psi), and 10.3 MPa (1,500 psi). These confined compressive strength tests were conducted at a temperature of 20°C (68°F) in axial strain control at an axial strain rate of $1 \times 10^{-4} \text{ s}^{-1}$.

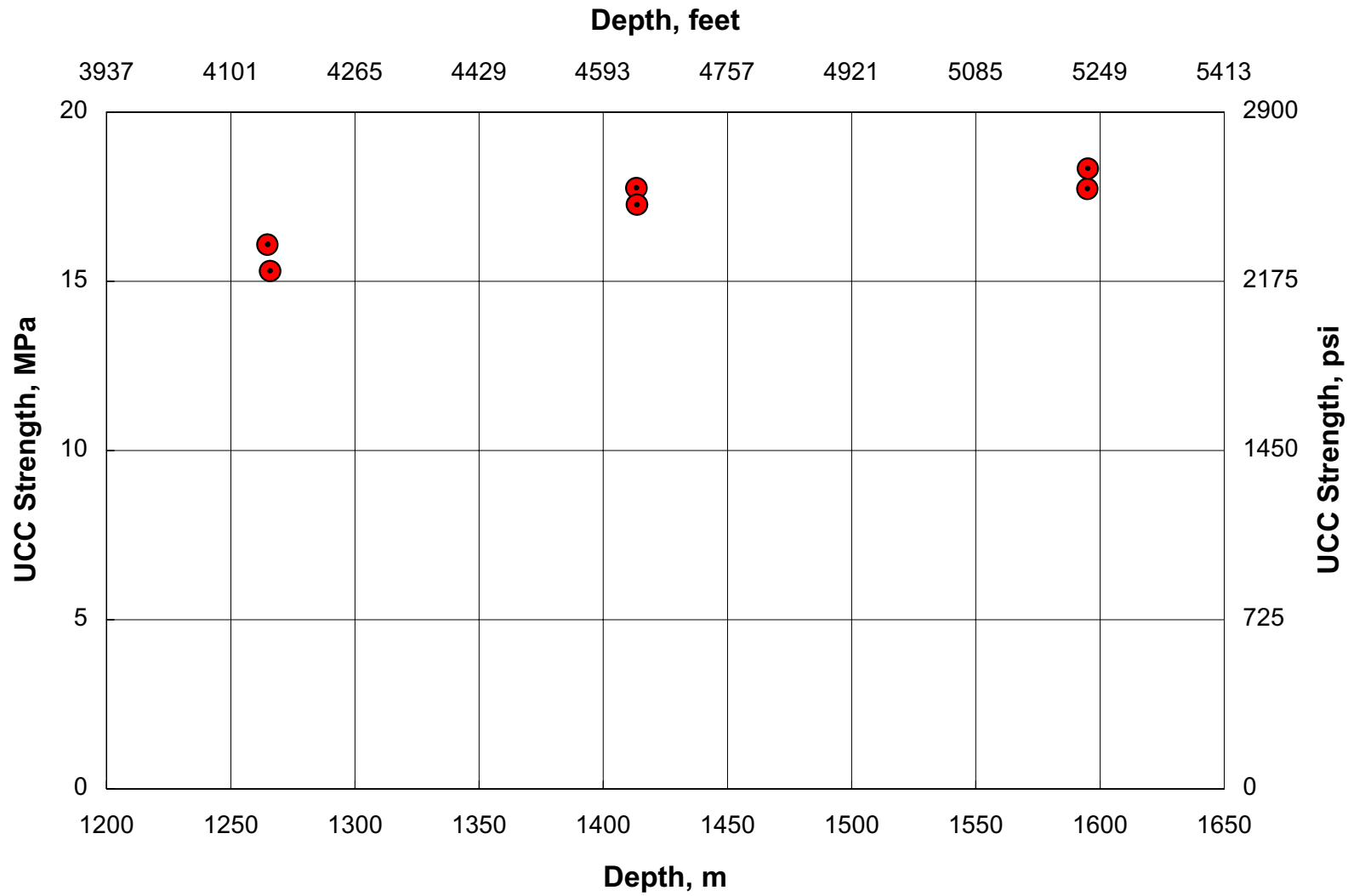


Figure 3-6. Unconfined Compressive Strength as a Function of Depth.

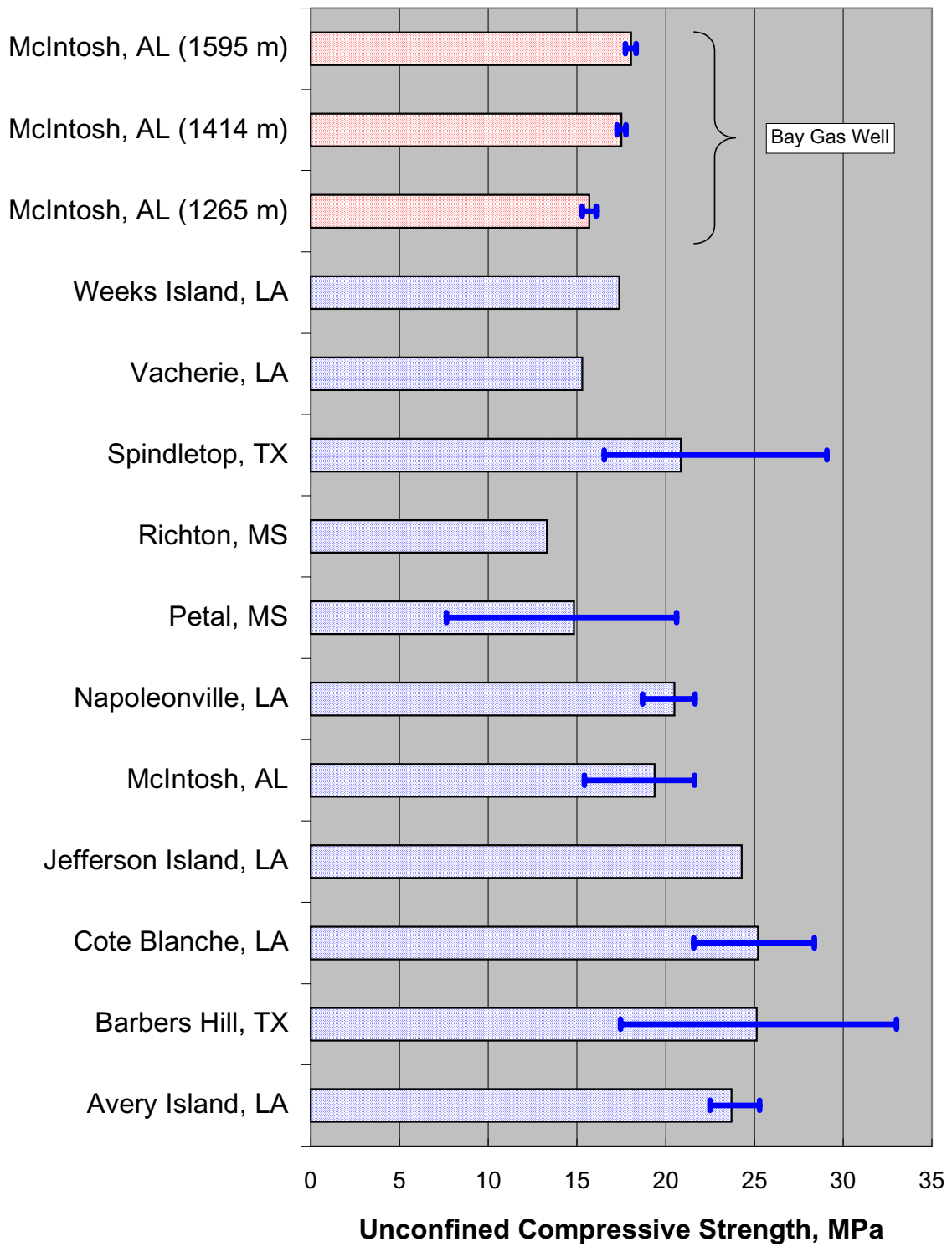


Figure 3-7. Comparison of Unconfined Compressive Strength of Various Salts.

Table 3-3. Unconfined Quasi-Static Compressive Elastic Constants

Specimen I.D.	Depth		Young's Modulus, E		Poisson's Ratio, ν
	(m)	(ft)	(GPa)	(psi)	
MD/BG2/4149.8	1,265	4,149.8	22.0	3,188,550	>0.5
MD/BG2/4153.0	1,266	4,153.0	19.6	2,844,939	0.387
MD/BG2/4637.1	1,413	4,637.1	14.6	2,120,000	0.387
MD/BG2/4637.7	1,414	4,637.7	19.3	2,793,668	>0.5
MD/BG2/5232.9	1,595	5,232.9	20.8	3,019,017	0.422
MD/BG2/5233.6	1,595	5,233.6	21.0	3,046,851	>0.5
Averages			19.6	2,835,504	0.398

Table 3-4 provides a summary of the unconfined compressive strengths determined from the six tests. As expected, the confined compressive strengths increased with increasing confining pressure, ranging from a strength of about 28 MPa (4,060 psi) at the lowest confining pressure of 1.0 MPa (150 psi) to a strength of about 43 MPa (6,240 psi) at the highest confining pressure of 10.3 MPa (1,500 psi).

Table 3-4. Summary of Confined Constant Strain Rate Strength Tests

Specimen I.D.	Depth		Confining Pressure		Strength	
	(m)	(ft)	(MPa)	(psi)	(MPa)	(psi)
MD/BG2/4128.4	1,258	4,128.4	5.2	750	43.6	6,323
MD/BG2/4130.7	1,259	4,130.7	10.3	1,500	46.3	6,715
MD/BG2/4134.3	1,260	4,134.3	1.0	150	26.2	3,804
MD/BG2/4134.6	1,260	4,134.6	5.2	750	35.2	5,105
MD/BG2/4136.9	1,261	4,136.9	1.0	150	29.3	4,252
MD/BG2/4158.0	1,267	4,158.0	10.3	1,500	41.0	5,940

All of the specimens in Table 3-5 incorporated unload/reload cycles in their load paths to generate data for estimating values of Young's modulus and Poisson's ratio. The elastic constants obtained from the tests are given in Table 3-5. The average value of Young's modulus was 27.1 GPa (3,935,188 psi) and the average value for Poisson's ratio was 0.321. The elastic constant values determined from the CSR tests are significantly different than the values

determined from the UCC tests. Moreover, the values determined using the CSR tests are more representative of typical values expected for salt. The large crystal size effect that was cited as the cause of spurious results in the UCC tests is apparently reduced when elevated confining pressures are applied.

Table 3-5. Constant Strain Rate Elastic Constants

Specimen I.D.	Depth		Young's Modulus, E		Poisson's Ratio, ν
	(m)	(ft)	(GPa)	(psi)	
MD/BG2/4128.4	1,258	4,128.4	28.4	4,112,756	0.288
MD/BG2/4130.7	1,259	4,130.7	29.5	4,272,635	0.309
MD/BG2/4134.3	1,260	4,134.3	23.6	3,425,700	0.369
MD/BG2/4134.6	1,260	4,134.6	28.2	4,092,686	0.304
MD/BG2/4136.9	1,261	4,136.9	23.7	3,434,460	0.344
MD/BG2/4158.0	1,267	4,158.0	29.5	4,272,953	0.309
Averages			27.1	3,935,198	0.321

3.5.4 Confined Constant Mean Stress Tests

Six confined constant mean stress dilation tests were performed on specimens obtained from a nominal depth of 1,265 meters (4,150 feet). Tests were terminated when the confining pressure had been completely removed (i.e., tensile radial stresses cannot be induced in the test specimen with this test configuration).

The data from the CMS tests were analyzed to identify the combinations of mean stress and stress difference that would initiate salt dilation. These data pairs were then cast in terms of the stress invariants J_2 and I_1 , and the results are summarized in Tables 3-6 and 3-7 (Table 3-6 presents results in SI units and Table 3-7 uses English units).

The intent of performing CMS tests was to compare the dilation characteristics of the salt with a typical criterion developed by Van Sambeek et al. [1993] for Avery Island Dome salt and southeastern New Mexico bedded salt as:

$$\frac{\sqrt{J_2}}{I_1} = 0.27 \quad (3-6)$$

This comparison is shown in Figure 3-8 where the dilation data from the CMS tests has been overlain on the typical criterion. The comparison is not good. The explanation for this unexpected result is believed to lie with the large crystals encountered in the Bay Gas salt. The

premise of the CMS test is that dilation begins with small microcracks that initiate along crystalline boundaries. When there are a large number of such boundaries available in the specimen (such as seen in specimens with small crystal sizes), the CMS test is a reliable indicator of dilation potential. The Bay Gas salt has very large crystals, so there are relatively few crystalline boundaries on which microcracking can initiate, and the large crystals may well be rotating or deforming in a manner that preempts the observation of the usual dilation stress limit. As a result, the CMS results on Bay Gas salt are considered suspect and additional analyses using dilation data that may be available from creep tests and CSR tests will be attempted.

Table 3-6. Summary of CMS Test Results (SI Units)

Specimen I.D.	Depth (m)	Mean Stress (MPa)	Dilation Stress (MPa)	I_1 (MPa)	$\sqrt{J_2}$ (MPa)
MD/BG2/4127.7	1,258	6.9	9.66	20.7	5.58
MD/BG2/4191.0	1,277	13.8	17.9	41.4	10.3
MD/BG2/4139.8	1,262	20.7	20.7	62.1	12.0
MD/BG2/4136.0	1,261	6.9	15.2	20.7	8.78
MD/BG2/4191.7	1,278	13.8	20.7	41.4	12.0
MD/BG2/4135.3	1,260	20.7	23.4	62.1	13.5

Table 3-7. Summary of CMS Test Results (English Units)

Specimen I.D.	Depth (ft)	Mean Stress (psi)	Dilation Stress (psi)	I_1 (psi)	$\sqrt{J_2}$ (psi)
MD/BG2/4127.7	4,127.7	1,000	1,400	3,000	808
MD/BG2/4191.0	4,191.0	2,000	2,600	6,000	1,501
MD/BG2/4139.8	4,139.8	3,000	3,000	9,000	1,732
MD/BG2/4136.0	4,136.0	1,000	2,200	3,000	1,270
MD/BG2/4191.7	4,191.7	2,000	3,000	6,000	1,732
MD/BG2/4135.3	4,135.3	3,000	3,400	9,000	1,963

3.5.5 Creep Tests

Six confined creep tests were completed or were in progress during the reporting period. All of the specimens were taken from a nominal depth of 1,265 meters (4,150 feet). These tests are

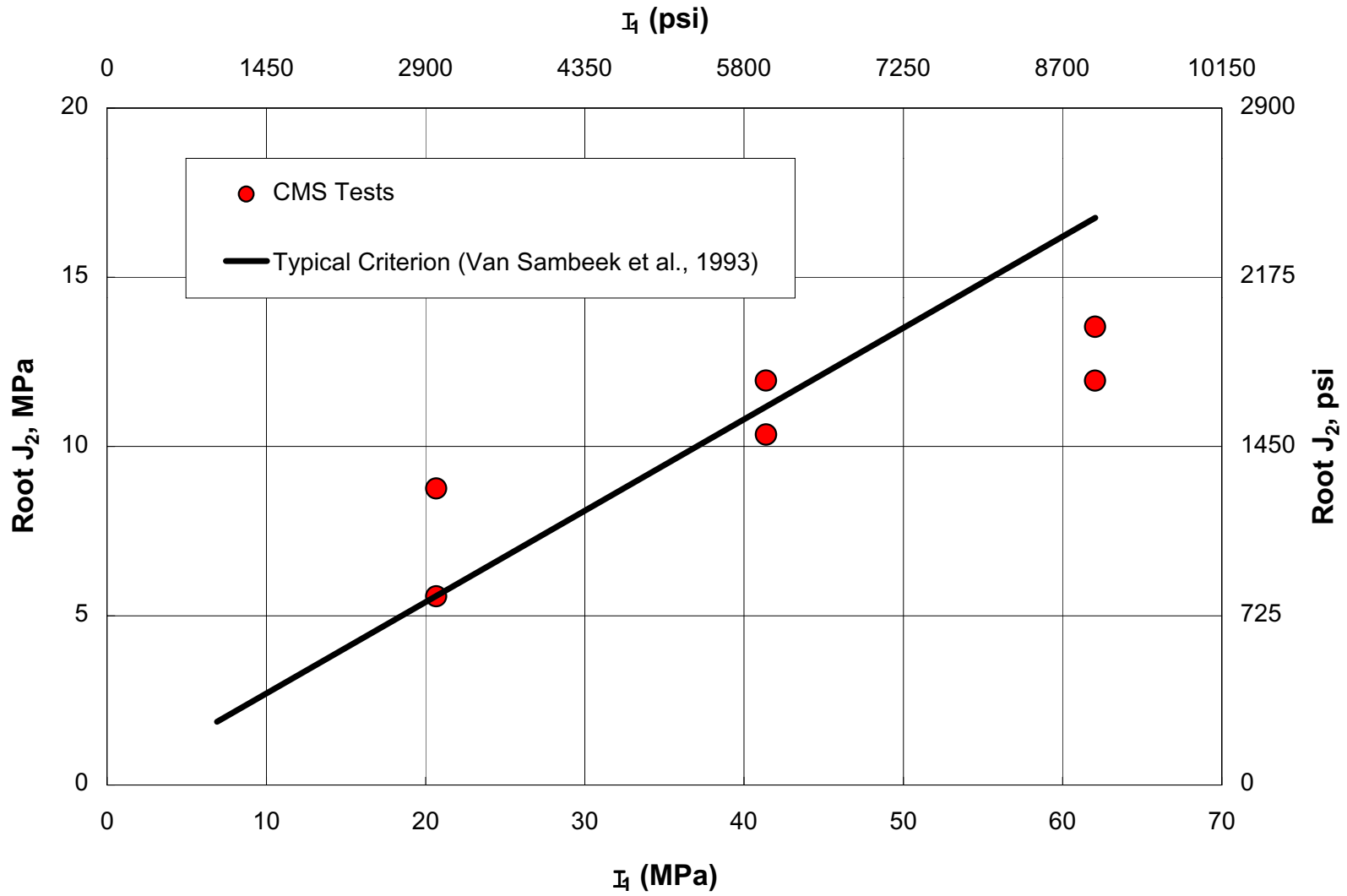


Figure 3-8. Dilation Criterion Comparison.

the first to be performed in an effort to complete a comprehensive matrix of creep tests. The comprehensive test matrix will require several more months to complete. All creep tests were conducted at a temperature of 52°C (125°F) because that temperature was considered to be a reasonable approximation of the anticipated average cavern temperature at its proposed midheight. A summary of the current creep tests is given in Table 3-8.

Table 3-8. Creep Test Matrix^(a)

Specimen I.D.	Depth		Stress Difference		Confining Pressure	
	(m)	(ft)	(MPa)	(psi)	(MPa)	(psi)
MD/BG2/4145.8	1,264	4,145.8	20.7	3,000	27.6	4,000
MD/BG2/4146.5 ^(b)	1,264	4,146.5	13.8	2,000	27.6	4,000
MD/BG2/4148.2 ^(b)	1,264	4,148.2	13.8	2,000	2.1	300
MD/BG2/4153.5	1,266	4,153.5	10.3	1,500	27.6	4,000
MD/BG2/4155.0	1,266	4,155.0	10.3	1,500	2.1	300
MD/BG2/4156.3 ^(b)	1,267	4,156.3	20.7	3,000	2.1	300

(a) All tests performed at a temperature of 52°C (125°F).

(b) Indicates tests that are in progress. Other tests are complete.

Although the creep testing has just begun and conclusions would be highly preliminary, a comparison of the current tests can be carried out. The data obtained from the last 2 days of each completed creep test were fitted to estimate values for steady-state strain rates. The values of the steady-state strain rate estimates obtained from the tests are given in Table 3-9 along with the applied axial stress differences.

Table 3-9. Steady-State Strain Rate Estimates

Specimen I.D.	Depth		Stress Difference		Steady-State Strain Rate Estimate (s ⁻¹)
	(m)	(ft)	(MPa)	(psi)	
MD/BG2/4145.8 ^(a)	1,264	4,145.8	20.7	3,000	5.45×10^{-8}
MD/BG2/4153.5 ^(a)	1,266	4,153.5	10.3	1,500	5.29×10^{-10}
MD/BG2/4155.0 ^(b)	1,266	4,155.0	10.3	1,500	1.77×10^{-9}

(a) Confining pressure was 27.6 MPa (4,000psi).

(b) Confining pressure was 2.1 MPa (300 psi).

The type of data presented in Table 3-9 can be used to evaluate how strongly the steady-state strain rates depend on changes in the applied axial stress difference. There is insufficient data available now to make any conclusions, but a simple example illustrates the process. A simple model relating the steady-state creep strain rate, $\dot{\epsilon}_s$, to the imposed stress difference is a power law that is expressed by:

$$\dot{\epsilon}_s = A(\Delta\sigma)^n \quad (3-7)$$

where $\Delta\sigma$ is the imposed stress difference, n is the stress exponent, and A is a fitting parameter. If the power law equation is transformed using logarithms, the following expression is obtained:

$$\log \dot{\epsilon}_s = \log A + n \log(\Delta\sigma) \quad (3-8)$$

The logarithmic equation is a linear equation in the transformed steady-state strain rate versus stress difference space and the stress exponent, n , represents the slope of the line in logarithmic space.

If the first two tests in Table 3-9 are fitted with Equation 4-3, the resulting slope of the fitted line is about $n = 6$. The third test is not included in the fit because it was performed at a very low confining pressure and the specimen exhibited dilational behavior. As a result of the dilation, the strain rate in the third test may not be representative of intact salt behavior. A comparison of the second test (high confining pressure) and third test (low confining pressure) suggests that the dilating specimen may exhibit much higher strain rates, even though both specimens were subjected to the same axial stress difference. At present, a robust determination of the stress dependence of the steady-state strain rate is unavailable because only two test results are included in the linear regression fit. However, after the complete test matrix is executed, there will be a much larger data set available for estimation of the stress dependence parameter, n .

4.0 PARAMETER EVALUATION

The MDCF model contains 42 model parameters that must be determined before a geomechanical modeling study can be performed of the gas storage caverns at the McIntosh Dome. The goal of the parameter evaluation task is to determine values for the parameters of the MDCF model that accurately describe the creep and plastic behavior of the salt at the McIntosh Dome. This chapter describes the technical approach for determining the parameter values of the MDCF model and selected results currently available at the time this report was written.

4.1 TECHNICAL APPROACH

Because the MDCF model contains numerous parameters, it is not practical to determine all the parameters simultaneously using the entire database of laboratory test results. The technical approach followed was to break down the problem into several smaller and more manageable least-squares analyses; wherein, only a few parameters are determined from any single analysis. Parameter values are determined based on the result that produces the lowest sum-of-squares error between the measured and predicted responses (either stress or strain). The steps to determine parameter values of the MDCF model include:

1. Identify those parameters that are deterministic.
2. Group parameters into sets that can be determined independently from other parameters in the model.
3. Identify prerequisites, if any, to determine parameters from each set (functional group of parameters).
4. Identify laboratory tests that can be used to determine the parameters in each functional group.
5. Develop software that includes the MDCF response models for the different laboratory load paths and responses (i.e., axial strain, volumetric strain, dilation stress).
6. Compile and organize the laboratory data into databases that are compatible with the nonlinear curve fitting software.
7. Assign weighting to each data point to reduce bias in the database. The goal is to reduce the bias of the fitting procedure with respect to strain magnitude such that the model will fit the low strain data equally as well as the larger strain data.
8. Select appropriate order for evaluating each parameter functional group based on prerequisites.
9. Perform least-squares analyses to determine values for free parameters.

4.2 NUMERICAL ROUTINES

Nonlinear curve fitting techniques are being used to determine site-specific parameter values for the MDCF model. The curve fitting techniques utilize the least-squares solution methodology to minimize the difference between the measured and predicted response. Two different least-squares solution programs were developed to determine parameter estimates for the MDCF model. The first uses Microsoft's spreadsheet program Excel employing the built-in *Solver* function in user designed worksheets. The second program was developed using the Fortran programming language and is considerably more robust. Selection of which program to use for a particular analysis depended on the size and complexity of the problem. Relatively small and simple problems could be solved more efficiently using Excel; whereas, the Fortran software program is better suited for computations involving time-dependent behavior and numerical integration.

4.3 MODEL FITTING

The highly nonlinear functions comprising the MDCF model make parameter value determination an arduous process. A strategy was outlined that will be used to determine the parameter values of the MDCF model. This strategy is based on the concept of fitting the model to the measured responses of laboratory tests that isolate material behavior that is characterized by a limited number of parameter values. For example, parameters that define steady-state creep can be determined from data measured at the end of long-term, high-confining-pressure creep tests when no other deformation mechanisms (e.g., elastic or brittle) are operative. Also, it was determined by Nieland et al. [1999] that a number of the parameters can be treated as deterministic while others do not contribute significantly to the deformation under the loading conditions experienced in the salt surrounding natural gas storage caverns during operation.

Table 4-1 lists both the free and deterministic parameters according to their role in the MDCF model. Free parameters will be determined based on laboratory tests performed on salt core recovered from the McIntosh Dome. The remaining parameters will be treated as deterministic and assigned the same values as those determined for the salt at the WIPP [Munson et al., 1989].

Some of the parameters were classified as deterministic because they have little influence on the predicted response of the salt surrounding a natural gas storage cavern. This is because the MDCF model was initially developed to predict the extreme conditions at a nuclear waste repository in salt. The stress and temperature conditions experienced in the salt during cavern storage are not within the regime where dislocation climb and glide dominate. As a result, parameters describing these mechanisms were classified as deterministic (B_1 , B_2 , q , A_1 , n_1). Because of the relatively small change in temperature over the height of the storage caverns,

parameters controlling the temperature dependency have little influence and are considered deterministic (Q_1/R , Q_2/R , c). Others parameters have a theoretical basis (m , σ_0) or are determined by mineralogy (ρ). Parameters associated with the development of cleavage fractures (x_1 , x_{3p} , ξ , x_4) under tensile stress states were not evaluated in this project because design constraints do not permit tension within the salt formation surrounding a cavern.

Table 4-1. Functional Groups of MDCF Parameters

Function	Free Parameters	Deterministic Parameters
Transient Creep	$\alpha, \beta, K_0, \alpha', \beta'$	m, c
Steady-State Creep	A_2, n_2	$B_1, B_2, q, A_1, n_1, Q_1/R, Q_2/R, \mu, \sigma_0,$
Shear Damage Strain Rate	$x_{3s}, c_0, c_2, c_3, n_3,$	$\omega_0,$
Damage Variable Rate ^(a)	ξ_s^1, ξ_s^2, x_4	t_0, ρ
Tension Damage ^(a)		x_1, x_{3p}, ξ, x_4
Healing	k_1, τ_0, τ_1	
Dilation Stress Boundary ^(a)	$x_2, x_{6s}, p_1,$	x_7, ρ
Damage Flow Potential	x_2, x_8	
Transient Damage	c_4, c_5	

(a) Note: the parameters x_2 , x_4 , and ρ belong to more than one functional group.

The parameters x_7 , t_0 , and μ are normalizing constants used to provide the correct dimensional units of time and stress, respectively. Selection of values for these two parameters is arbitrary since other parameters in the model will adjust proportionally to produce the same least-squares solution. To remain consistent with the original developers of the MDCF, x_7 is set equal to 1 MPa, t_0 is set equal to 1 second, and μ is given the value for the shear modulus of salt at the McIntosh Dome. Similarly, ω_0 is assigned a negligible value of 0.001 since the damage rate equation requires a nonzero initial value.

Of the 42 parameters identified in Table 4-1, only 24 site-specific parameters are required to predict the behavior of salt caverns during natural gas storage at the McIntosh Dome. The 24 parameters were organized into nine functional groups, as shown in Table 4-1. At the time of this report, preliminary values have been determined for the three functional groups identified as: (1) transient creep, (2) steady-state creep, and (3) dilation stress boundary. Comparison between the measured and predicted responses used to determine parameter values for these three groups is provided in the next section.

4.4 MDCF RESPONSE MODEL FIT

Steady-state and transient creep parameters ($A_2, n_2, \alpha, \beta, K_0, \alpha_r, \beta_r$) were determined from three creep tests subject to a confining pressure of 27.6 MPa (4,000 psi) and stress differences of 10.3, 13.8, and 20.7 MPa (1,500, 2,000, and 3,000 psi). Before fitting the response model to the axial strain versus time data, the raw data collected in the laboratory was reduced and limited to 100 points per test. The procedure used to select the 100 data points from each test was based on an incremental time interval. The procedure was developed to ensure that the first and last data points in each test are included with data points at nearly equal time intervals in between.

Figure 4-1 compares the MDCF model prediction to the three laboratory creep tests performed at a confining pressure of 27.6 MPa (4,000 psi) identified in Chapter 3.0. The model does an excellent job of predicting the steady-state strain rates over the range of stress differences tested. The predicted transient strain response is considered good for these three tests; however, significantly more strain was predicted for the test performed at a stress difference of 13.8 MPa (1,500 psi) than was measured in the laboratory. The difference between the measured and predicted response is believed attributable to the transient strain response of the salt at low stress differences. Further investigations will have to be performed to identify the adequacy of the transient response of McIntosh Dome salt.

MDCF model parameters that define the damage effective stress measure (x_2, x_6, ρ_1) were determined using the results of the six CMS tests described in Chapter 3.0. Figure 4-2 shows the dilation boundary predicted by the model under conditions of a triaxial compression test (i.e., $\sigma_z > \sigma_x = \sigma_y$). The results shown in Figure 4-2 are presented in terms of the first invariant of the Cauchy stress tensor, I_1 , and the second invariant of the deviatoric stress tensor, $\sqrt{J_2}$. These two stress measures are defined as follows:

$$I_1 = \sigma_1 + \sigma_2 + \sigma_3 \quad (4-1)$$

$$\sqrt{J_2} = \left(\frac{1}{6} \left[(\sigma_1 - \sigma_2)^2 + (\sigma_1 - \sigma_3)^2 + (\sigma_2 - \sigma_3)^2 \right] \right)^{\frac{1}{2}} \quad (4-2)$$

where:

$\sigma_1, \sigma_2,$ and $\sigma_3 =$ principal stress.

Bay Gas Creep Tests

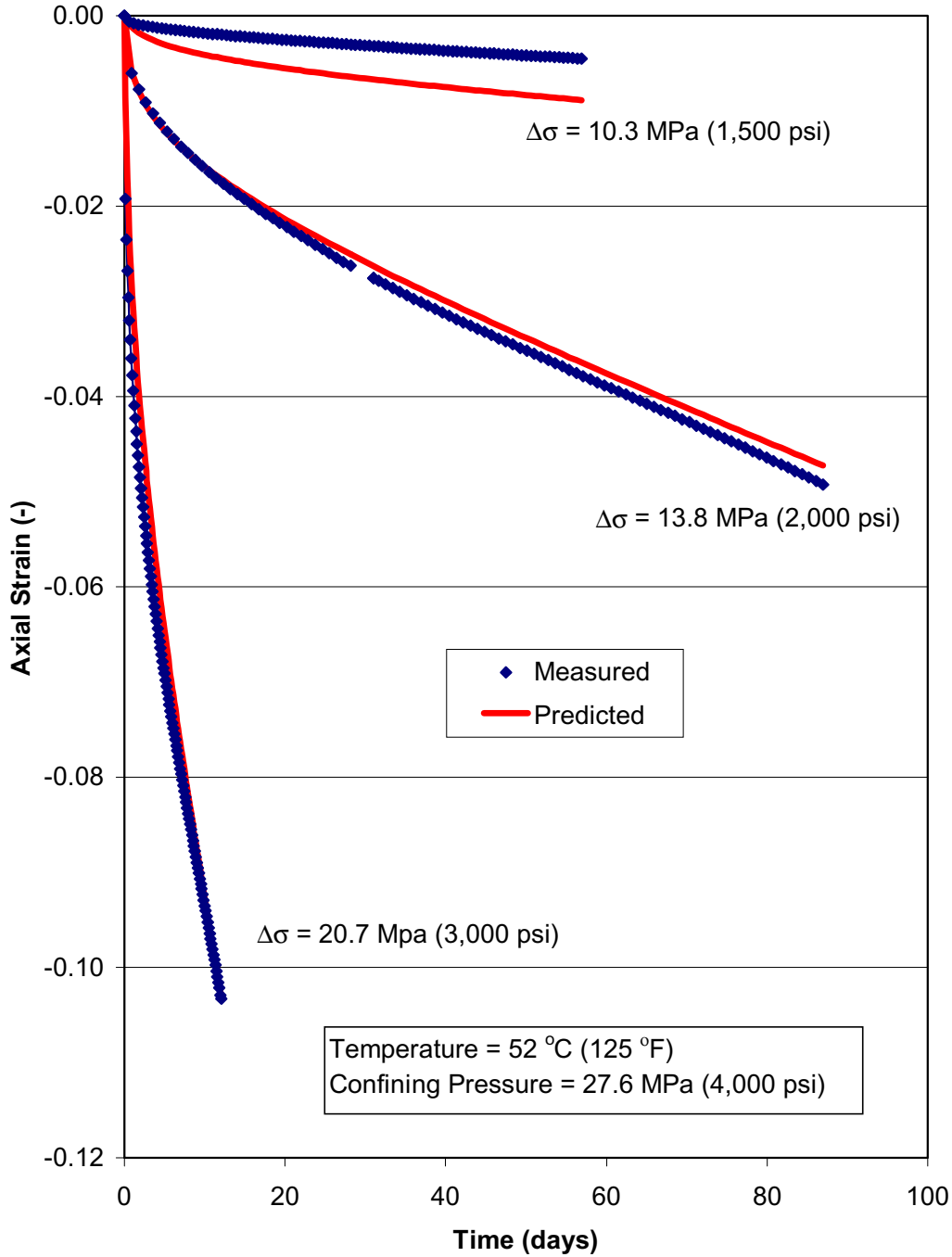


Figure 4-1. Comparison of Measured and Predicted Creep Tests Performed on Salt From Bay Gas Well No. 2 at 52°C (125°F) and 27.6 MPa (4,000 psi) Confining Pressure.

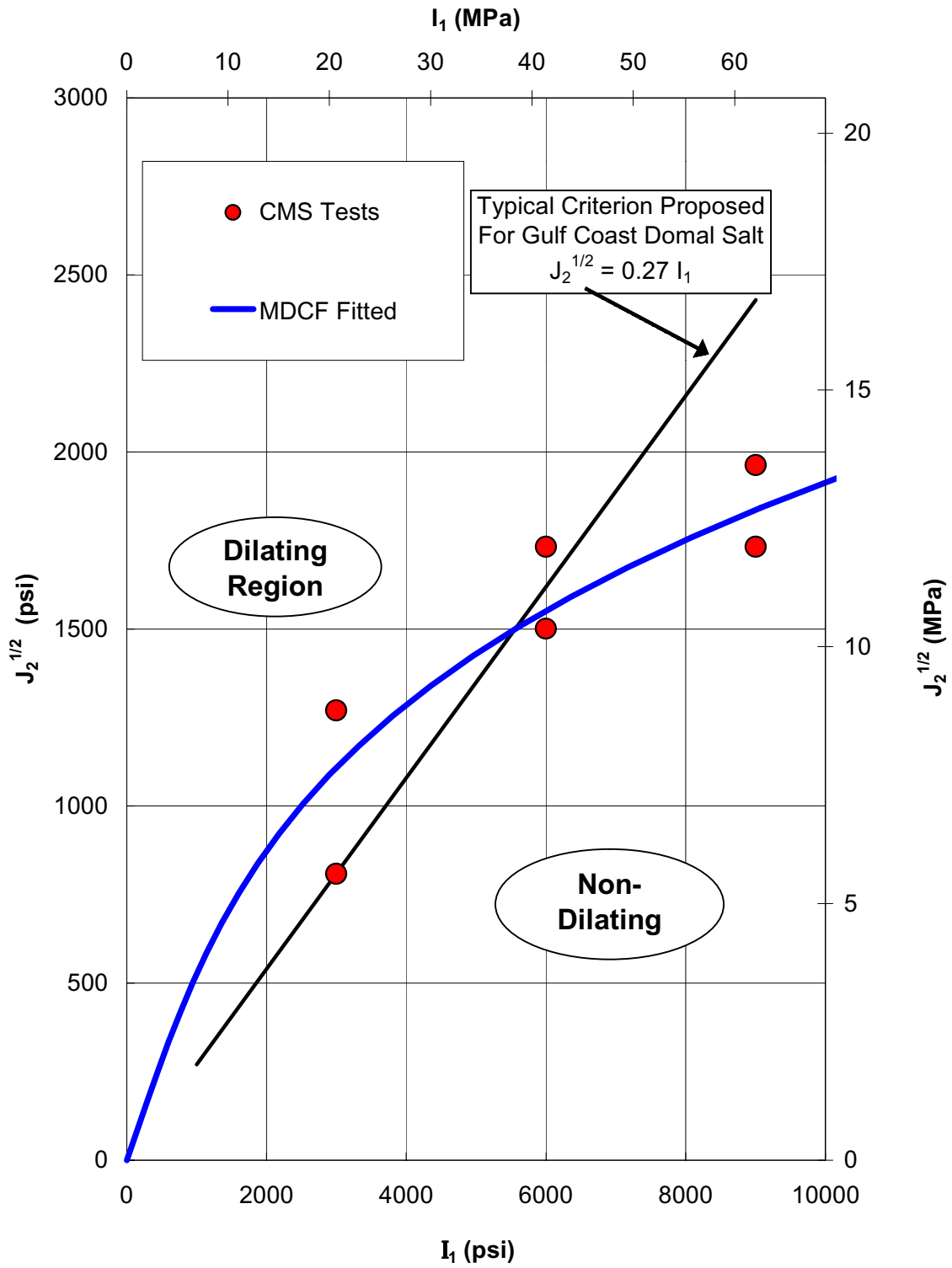


Figure 4-2. Comparison of Measured and Predicted Stress States for the Onset of Dilation.

The MDCF dilation boundary indicates that the dilation stress increases with mean stress (or I_1) and divides the $\sqrt{J_2}$ -versus- I_1 stress space into two regions. The region below and to the right of the line represents a *nondilating* region. Conversely, the region above and to the left of the line represents a *dilating* region. Also shown in Figure 4-2 are the dilational stresses determined from the six CMS tests described in Chapter 3.0 and the dilation limit proposed for other Gulf Coast salts [Van Sambeek et al., 1993] given by the following linear relationship referred to as the damage potential:

$$\sqrt{J_2} \leq 0.27 I_1 \quad (4-3)$$

As shown in Figure 4-2, the dilation boundary predicted by the MDCF model is different than the linear dilation boundary given by the Damage Potential relationship. The MDCF model dilation limit is greater than the Damage Potential relationship for values of $\sqrt{J_2}$ less than 10.3 MPa (1,500 psi) but becomes significantly lower than the Damage Potential relationship for $\sqrt{J_2}$ greater than 10.3 MPa (1,500 psi). The results presented in Figure 4-2 for the MDCF model are for triaxial compression stress states and will most likely be different at other stress conditions, such as triaxial extension (i.e., $\sigma_{zz} < \sigma_{xx} = \sigma_{yy}$).

5.0 DISCREPANCY RESOLUTION AND MODEL REFINEMENT

The MDCF model was developed for the extreme conditions of a nuclear waste repository in salt. The continuous change in the state of stress for the salt surrounding a natural gas storage cavern when gas is injected and withdrawn was not a consideration during the development of the model. Additionally, development of the model ceased before the healing term in the model was complete. As a result, discrepancy resolution and model refinement activities were considered necessary in this first-time application of the salt damage criterion to correct known deficiencies associated with damage recovery (healing) and address other potential unforeseen problems. It was envisioned that discrepancy resolution and model refinement would involve two components: (1) a laboratory testing component to refine the description of the healing mechanisms and (2) a theoretical component to develop mathematical descriptions for the healing mechanisms, to correct known deficiencies in the healing model, and to implement the changes into our numerical analysis software so the cavern calculations can be performed.

Activities were initiated to develop a technically sound and feasible approach for implementing directional flow during damage healing using the finite element method. During the course of this work, the possibility of changing the power-conjugate effective stress measures for shear-induced damage was contemplated. Healing term refinements have been implemented into the finite element program SPECTROM-32 [Callahan et al., 1989]; however, only theoretical considerations have been given to updating the power-conjugate effective stress measures for shear-induced damage. These issues are discussed separately in the next two sections.

5.1 MDCF MODEL HEALING TERM REFINEMENTS

The MDCF damage accumulation model includes stress-induced anisotropy by virtue of the effective stress measure used to describe the flow potential. Thus the volumetric bulking or dilation occurs normal to the minor principal stress (with compression assumed to be negative) representative of microfracturing occurring in the material. As presently written [Chan, 1996], the damage recovery or healing portion of the model also relies on a stress-induced anisotropy formulation without any knowledge of prior damage accumulation. Thus under certain conditions, damage recovery could be occurring in directions inconsistent with the original damage accumulation. This could occur if the principal stress directions change between the time when damage accumulates and damage recovery occurs. In addition, the damage recovery is indeterminate under hydrostatic states of stress, predicts axial shortening under triaxial extension conditions, and predicts axial lengthening under triaxial compression conditions. To alleviate these difficulties, an isotropic flow potential was initially adopted, which was subsequently implemented into the finite element program SPECTROM-32. However, the isotropic flow condition also suffers deficiencies since the flow is the same in every direction. In fact,

with fixed boundaries or under plane-strain conditions, large tensions may be produced with the isotropic flow potential when damage recovery occurs.

To alleviate these flow potential problems during damage recovery or healing, the stress normal to the initial damage accumulation was adopted for this proof-of-concept project as the effective stress governing the flow potential. The assumption used is that microfractures will be generated parallel to the minor principal stress and that further damage accumulation will not alter the orientation of the microfractures. Subsequently, when and if conditions for damage recovery occur, the recovery (crack closure and sintering) will occur normal to the microfractures as dictated by the orientation of the damage. Thus the flow potential for damage recovery is written as a function of the normal stress occurring on the oriented microfractures. The mathematical formulation for the healing portion of the MDCF model is presented in Appendix A, along with the development of the flow potential based on the stress normal to the microfractures.

5.2 ALTERNATIVE FORMULATION OF THE POWER-CONJUGATE EQUIVALENT STRESS MEASURES FOR SHEAR-INDUCED DAMAGE

The MDCF constitutive model evolved as additional laboratory test data became available. Initially, the model was described by Chan et al. [1992]. Since that time, the damage model has been updated as proposed by Chan [1993], Chan et al. [1995; 1996], and Chan [1996]. Unfortunately, the prior development and refinement of the MDCF model has relied primarily on triaxial compression states of stress. Analyses of underground caverns typically result in states of stress other than triaxial compression. Because it is possible that salt may be weaker or behave differently at stress states other than triaxial compression, alternative formulations of the power-conjugate equivalent stress measures for shear-induced damage were developed as a possible update to the MDCF model. The impetus of this work is motivated by the possibility that the minimum allowable gas pressure determined using the MDCF model may not be conservative because it was developed using tests performed solely under triaxial compression states of stress.

Appendix B provides a review of rock behavior under states of stress common in underground caverns other than triaxial compression and introduces a potential modification to the power-conjugate equivalent stress measures for shear-induced damage. A limited number of laboratory tests are planned using triaxial extension states of stress under this project. If the results of these tests indicate significantly different responses for triaxial compression and triaxial extension states of stress, the modification will be incorporated into the MDCF model and SPECTROM-32. However, confidence in the model's ability to predict the behavior of salt under conditions other than triaxial compression states of stress may be compromised because of the limited amount of data.

6.0 CAVERN ANALYSES

Geomechanical modeling is used to predict cavern stability and performance during development and under various operating scenarios during natural gas storage. The information obtained from the site investigation and laboratory testing is incorporated into finite element or finite difference models that are representative of the cavern and its surroundings. The allowable minimum and maximum operating pressure are established from the numerical simulations based on the following performance criteria:

- The minimum operating pressure will not result in salt dilation (microfracturing). Extensive areas of salt dilation could lead to spalling of the roof and/or walls of the cavern and subsequent damage to the casing shoe, well, and/or hanging string.
- The minimum and maximum operating pressures will not result in connectivity with adjacent caverns or the flanks of the dome caused by tensile or hydraulic fracturing. Connectivity with adjacent caverns or the dome flank could produce an uncontrolled loss of the gas stored in the cavern.
- The operating pressure cycle will not cause excessive creep closure of the cavern. Creep closure progressively reduces the amount of gas that can be stored in a cavern, and excessive closure may require that the cavern be taken out of storage service prematurely and re-leached to increase its volume.
- The operating pressure cycle will not result in excessive surface subsidence. Creep closure results in progressive surface subsidence at the cavern site, which in turn, applies strain to well casing strings of the storage cavern and surrounding caverns and to surface structures, such as piping, buildings, and roads.

Model development of the Bay Gas storage caverns has been initiated. However, numerical simulations of the cavern cannot be completed until laboratory testing and parameter evaluation activities are complete. The next sections describe the progress that has been made in developing models that will be used to predict the behavior of existing and planned Bay Gas natural gas storage caverns.

6.1 BAY GAS WELL NO. 1 MODEL

All the information necessary to perform the numerical analysis of the Bay Gas Well No. 1 has been identified except for the material properties of the salt. A finite element mesh was generated that will be used for the geomechanical analysis of the Bay Gas Well No. 1 cavern. The two-dimensional axisymmetric representation was developed based on sonar data of the cavern taken in July 1994, immediately before the cavern was dewatered and put into service. At that time, the total cavern volume was approximately 432,000 cubic meters (2.71 MMbbls).

The finite element model was generated such that the volume of the cavern model replicated the actual volume of the cavern as determined by the sonar. This was accomplished by varying the cavern radius of the model with depth to match the volume versus depth computations obtained from the sonar data. Figure 4-2 presents an isometric view of the Bay Gas Well No. 1 cavern based on the July 1994 sonar. No apparent direction of preferential solutioning is observed for this cavern, which makes it ideally suited for representation by an axisymmetric model. Figure 6-1 presents the finite element mesh generated for this cavern.

6.2 BAY GAS WELL NO. 2 MODEL

All the information necessary to perform the numerical analysis of the Bay Gas Well No. 2 has been identified except for the material properties of the salt. Finite element mesh development of Bay Gas Well No. 2 has not been initiated. However, the model will be based on the solution-mining simulations that predict a cavern volume of 671,000 cubic meters (4.22 MMbbls) with a maximum radius of 73 meters (240 feet) and a height of about 305 meters (1,000 feet).

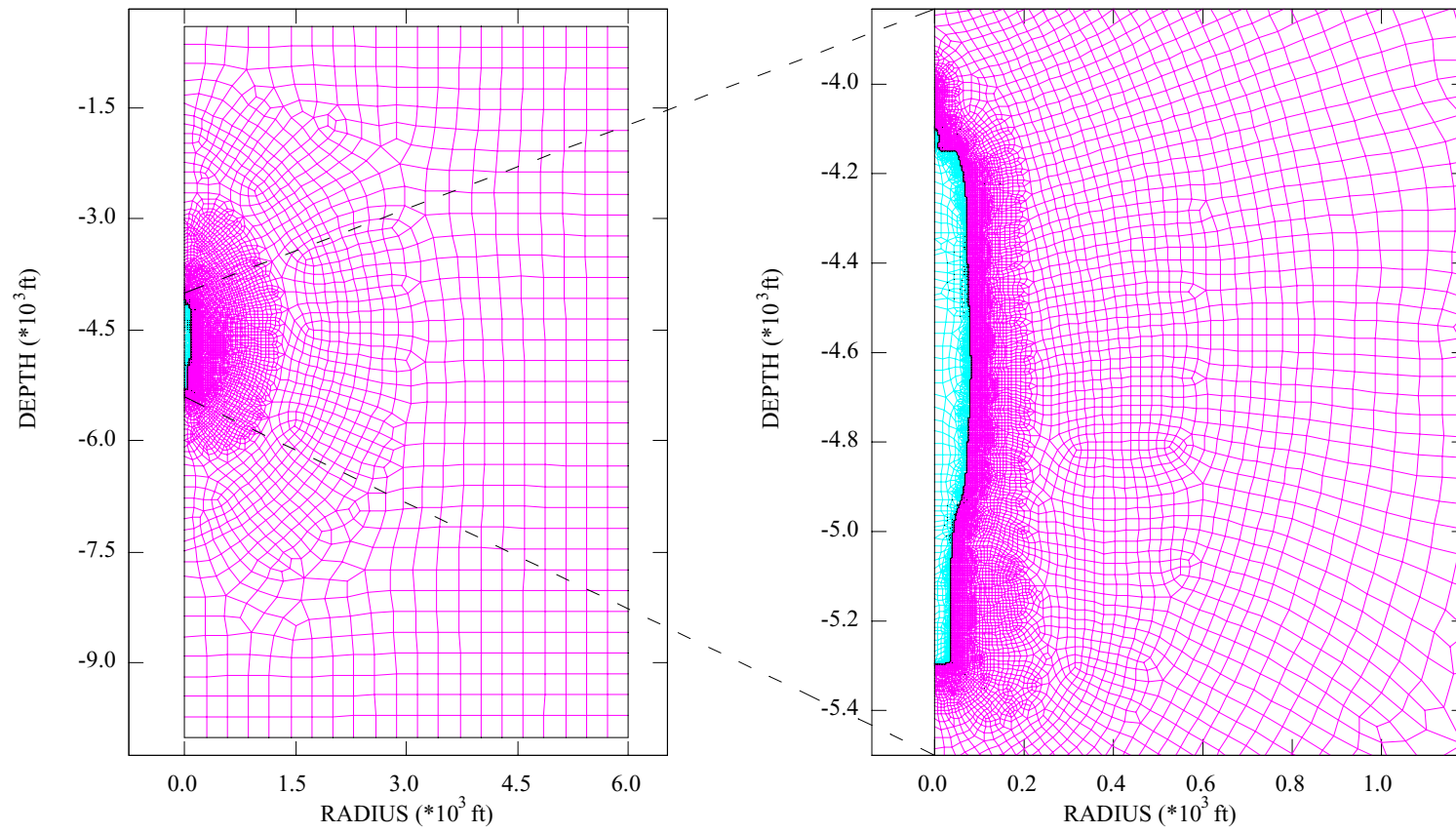


Figure 6-1. Two-Dimensional Axisymmetric Finite Element Model of the Bay Gas Well No. 1 Cavern.

7.0 SUMMARY

This report presents a summary of the activities that have been performed under DOE Contract DE-FC26-00NT41026 from October 1, 2000, through September 30, 2001. During this reporting period, activities were performed under all five project tasks.

Task 1 – *Site Characterization* is essentially complete. All site-specific information necessary to make a geomechanical analysis has been collected as well as salt core for material testing.

Task 2 – *Laboratory Testing* was initiated approximately 2 months behind plan. This delay was due largely to a later-than-anticipated spud date for Bay Gas Well No. 2. The quality of the data obtained to date is considered exceptional; however, testing will likely continue into January 2002.

In an effort to keep the project on schedule, work under Task 3 – *Parameter Evaluation* has been accelerated so that this task will be completed shortly after the laboratory testing task is complete. At the time of this report, 9 of the 24 free parameters of the MDCF model have been determined. The parameters determined describe the isochoric creep (both steady-state and transient) and salt dilation boundary. Parameters that describe the evolution of damage, healing, and recovery are yet to be determined.

One of the primary objects of Task 4 – *Model Refinement* was to update the healing portion of the MDCF model to correct known deficiencies and implement those changes into SPECTROM-32. This objective has been realized; however, planned laboratory testing to evaluate the healing portion of the model has not been undertaken. In addition to updating the healing term, new power-conjugate stress measures for shear-induced damage were formulated. Because most rocks behave differently in triaxial compression and extension with the material being weaker in extension, investigation of a new effective stress measure is being pursued.

Other than development of the finite element mesh representation of Bay Gas Well No. 1, little work has been, or can be, done under Task 5 – *Cavern Analysis* until after the parameter evaluation task is complete. According to the project management plan [DeVries, 2001], most of the work to be performed under this task is not scheduled to start until the second quarter of the 2002 government fiscal year (March 2002).

Other than the delay in receiving salt core, no unexpected problems have occurred that affect project cost or schedule. The upcoming year will answer the following questions regarding this proof-of-concept research:

1. Is the laboratory test matrix proposed by Nieland et al. [1999] sufficient to determine all the parameter values of the MDCF model necessary to evaluate natural gas storage in salt formations?
2. Was this proof-of-concept project successful in demonstrating a potential increase in the working gas capacity of an actual natural gas storage cavern using the salt damage criterion?

8.0 REFERENCES

Callahan, G. D., A. F. Fossum, and D. K. Svalstad, 1989. *Documentation of SPECTROM-32: A Finite Element Thermomechanical Stress Analysis Program*, DOE/CH/10378-2, prepared by RE/SPEC Inc., Rapid City, SD, for the U.S. Department of Energy, Chicago Operations Office, Argonne, IL, Vol. I and II.

Chan, K. S., 1993. *Further Development of Fracture Constitutive Model for Rock Salt*, Monthly Technical Report No. FY '93-8, prepared by Southwest Research Institute, San Antonio, TX, for Sandia National Laboratories, Albuquerque, NM, February.

Chan, K. S., 1996. *Final Development of the Multimechanism Deformation Coupled Fracture (MDCF) Constitutive Model*, Monthly Technical Report No. FY '96-2, Monthly Progress Report for Southwest Research Institute, Contract AQ-1458 with Sandia National Laboratories, February.

Chan, K. S., S. R. Bodner, A. F. Fossum, and D. E. Munson, 1992. "A Constitutive Model for Inelastic Flow and Damage Evolution in Solids Under Triaxial Compression," *Mechanics of Materials*, Vol. 14, pp. 1-14.

Chan, K. S., S. R. Bodner, A. F. Fossum, and D. E. Munson, 1995. "Constitutive Representation of Damage Healing in WIPP Salt," *Proceedings, 35th U.S. Symposium on Rock Mechanics*, University of Nevada, Reno, NV, June 5-7, J. J. K. Daemen and R. A. Schultz (eds.), A. A. Balkema, Rotterdam, pp. 485-490.

Chan, K. S., S. R. Bodner, D. E. Munson, and A. F. Fossum, 1996. "Inelastic Flow Behavior of Argillaceous Salt," *International Journal of Damage Mechanics*, Vol. 5, No. 3, pp. 292-314, July.

DeVries, K. L., 2001. *Management Plan for DOE Contract No. DE-FC26-00NT41026 Proof-of-Concept Research for an Advanced Design Criterion to Improve Working Gas Capacity for Natural Gas Storage Caverns in Salt Formations*, RSI-SIR-00-04, prepared by RESPEC, Rapid City, SD, for U.S. Department of Energy, Morgantown, WV.

DeVries, K. L., J. D. Nieland, and J. L. Ratigan, 1998. *Feasibility Study for Lowering the Minimum Gas Pressure in Solution-Mined Caverns Based on Geomechanical Analyses of Creep-Induced Damage and Healing*, RSI-0969, prepared by RESPEC, Rapid City, SD, for U.S. Department of Energy, Morgantown, WV.

Herrmann, W., W. R. Wawersik, and H. S. Lauson, 1980. “*Analysis of Steady-State Creep of Southeastern New Mexico Bedded Salt*,” SAND80-2172, Sandia National Laboratories, Albuquerque, NM.

Mellegard, K. D. and T. W. Pfeifle, 1998. “Laboratory Evaluation of Mechanical Properties of Rock Using an Automated Triaxial Compression Test With a Constant Mean Stress Criterion,” *Nondestructive and Automated Testing for Soil and Rock Properties*, ASTM STP 1350, W. A. Marr and C. E. Fairhurst (eds.), American Society for Testing and Materials, West Conshohocken, PA.

Mellegard, K. D. and P. E. Senseny, 1983. *Exponential-Time Creep Law for Avery Island Salt*, ONWI-329, prepared by RE/SPEC, Inc., Rapid City, SD, for the Office of Nuclear Waste Isolation, Battelle Memorial Institute, Columbus, OH.

Munson, D. E., A. F. Fossum, and P. E. Senseny, 1989. *Advances in Resolution of Discrepancies Between Predicted and Measured In Situ WIPP Room Closures*, SAND88-2948, Sandia National Laboratories, Albuquerque, NM.

Nieland, J. D., K. L. DeVries, and K. D. Mellegard, 1999. *Phase II Feasibility Study for Lowering the Minimum Gas Pressure in Solution-Mined Caverns Based on Geomechanical Analyses of Creep-Induced Damage and Healing*, RSI-1165, prepared by RESPEC, Rapid City, SD, for U.S. Department of Energy, Morgantown, WV.

Pfeifle, T. W., T. J. Vogt, and G. A. Brekken, 1995. *Correlation of Chemical, Mineralogic, and Physical Characteristics of Gulf Coast Dome Salt to Deformation and Strength Properties*, Research Project Report No. 94-004-S, prepared by RE/SPEC Inc., Rapid City, SD, for the Solution Mining Research Institute Inc., Woodstock, IL.

Ratigan, J. L., J. D. Nieland, and J. D. Osnes, 1993. “Rock Mechanics Aspects of Natural Gas Storage in Domal Salt,” *Solution Mining Research Institute Fall Meeting*, Lafayette, LA, October 25–26.

Van Sambeek, L. L., J. L. Ratigan, and F. D. Hansen, 1993. “Dilatancy of Rock Salt in Laboratory Test,” *Proceedings, 34th U.S. Symposium on Rock Mechanics*, University of Wisconsin-Madison, Madison, WI, June 27–30, B. C. Haimson (ed.), *International Journal of Rock Mechanics and Mining Sciences & Geomechanics Abstracts*, Pergamon Press, Vol. 30, No. 7, pp. 735–738.

APPENDIX A

REVISED MATHEMATICAL FORMULATION OF THE MDCF MODEL HEALING TERM

APPENDIX A

REVISED MATHEMATICAL FORMULATION OF THE MDCF MODEL HEALING TERM

A.1 DEVELOPMENT OF THE REVISED MDCF MODEL HEALING FORMULATION

The total inelastic strain rate in the MDCF model is represented by three components:

$$\dot{\epsilon}_{ij}^i = \dot{\epsilon}_{ij}^c + \dot{\epsilon}_{ij}^d + \dot{\epsilon}_{ij}^h \quad (\text{A-1})$$

The first inelastic strain rate represents climb-controlled creep; the second inelastic strain rate represents damage accumulation in the model; and the third inelastic strain rate represents healing in the model, which is our main interest. The kinetic equation representing the healing or damage recovery is written as:

$$\dot{\epsilon}_{ij}^h = \dot{\epsilon}_{eq}^h \frac{\partial \sigma_{eq}^h}{\partial \sigma_{ij}} \quad (\text{A-2})$$

where σ_{eq}^h and $\dot{\epsilon}_{eq}^h$ are the power-conjugate equivalent stress measure and the equivalent inelastic strain rate for the healing mechanism, respectively. The healing strain rate is written as:

$$\dot{\epsilon}_{eq}^h = \frac{\epsilon_{kk}^i (\sigma_{eq}^{h*} - \sigma_b) H(\sigma_b - \sigma_{eq}^{h*})}{\tau \mu} \quad (\text{A-3})$$

where ϵ_{kk}^i is the inelastic volumetric strain, τ is a characteristic time constant, and μ is the shear modulus. $H(\bullet)$ is the Heaviside function; thus, the healing rate is zero if the equivalent stress measure is less than σ_b . The addition of the Heaviside function is a modification of the form originally given by Chan et al. [1995a].¹ The equivalent stress measure (σ_{eq}^{h*}) used to describe the magnitude of the healing strain rate is different than the power-conjugate equivalent stress measure used to describe the flow potential (nonassociative formulation) and is given by:

$$\sigma_{eq}^{h*} = \frac{1}{3}(I_1 - \sigma_3) \quad (\text{A-4})$$

¹ Chan, K. S., S. R. Bodner, A. F. Fossum, and D. E. Munson, 1995. "Constitutive Representation of Damage Healing in WIPP Salt," *Proceedings, 35th U.S. Symposium on Rock Mechanics*, University of Nevada, Reno, NV, June 5–7, J. J. K. Daemen and R. A. Schultz (eds.), A. A. Balkema, Rotterdam, pp. 485–490.

where I_1 is the first invariant of the stress tensor and σ_3 is the minor (minimum) principal stress. The value for σ_b is determined from the shear-induced, power-conjugate equivalent stress measure for damage accumulation ($\sigma_{eq}^{\omega_s}$), which is written as:

$$\sigma_{eq}^{\omega_s} = |\sigma_1 - \sigma_3| + f_p x_2 x_7 \operatorname{sgn}(I_1 - \sigma_3) \left[\frac{I_1 - \sigma_3}{3x_7 \operatorname{sgn}(I_1 - \sigma_3)} \right]^{x_6} \quad (\text{A-5})$$

where σ_1 is the major (maximum) principal stress; x_2 , x_6 , and x_7 are material parameters; $\operatorname{sgn}(\bullet)$ represents the sign of its argument; and f_p is a material parameter related to the impurity content by:

$$f_p = 1 - p_1 \rho \quad (\text{A-6})$$

where ρ is the impurity content and p_1 is a material parameter. Solving for $\sigma_{eq}^{h^*}$ when $\sigma_{eq}^{\omega_s} = 0$ yields the value for σ_b ; viz,

$$\sigma_b = -x_7 \left[\frac{\sigma_1 - \sigma_3}{f_p x_2 x_7} \right]^{1/x_6} \quad (\text{A-7})$$

The quantity $\sigma_{eq}^{h^*} - \sigma_b$ coincides with the damage equivalent stress measure when $\sigma_{eq}^{\omega_s} = 0$ so that a distinct boundary exists between damage accumulation and damage recovery (healing), and the processes are noncompeting. The characteristic time constant is taken to be a function of the inelastic volumetric strain and is written as:

$$\tau = \tau_0 \exp(-k_1 \varepsilon_{kk}^i) + \tau_1 \quad (\text{A-8})$$

where k_1 , τ_0 , and τ_1 are material constants. When the volumetric strain is large, the exponential term becomes insignificant and the limiting value for τ is τ_1 . τ_1 is then the characteristic time associated with microcrack crack closure when the level of damage is high. When the inelastic volumetric strain becomes small, the limiting value of τ is $\tau_0 + \tau_1$, which is the characteristic time constant associated with crack sintering.

Damage (ω) is described in terms of an evolutionary equation as:

$$\dot{\omega} = \dot{\omega}_s + \dot{\omega}_t - h(\omega, \sigma_{eq}^{h^*}) \quad (\text{A-9})$$

where subscripts s and t represent the shear- and tension-induced damage accumulation rates, respectively, and h represents the damage recovery (healing) function. The healing portion of

the equation is taken from Chan [1996]¹ with a modification to halt healing when the material returns to its initial damage state:

$$h = \frac{\omega H(\omega - \omega_0) (\sigma_{eq}^h - \sigma_b) H(\sigma_b - \sigma_{eq}^h)}{\tau \mu} \quad (\text{A-10})$$

The stress normal to the initial damage accumulation is adopted as the effective stress measure governing the flow potential. The assumption used is that microfractures will be generated parallel to the minor principal stress and that further damage accumulation will not alter the orientation of the microfractures. Thus the principal stress angle (at the initiation of damage accumulation) defines the orientation of the damage. Subsequently, when and if conditions for damage recovery occur, the recovery (crack closure and sintering) will occur normal to the microfractures as dictated by the principal angle. Thus the power-conjugate equivalent stress measure (cf. Equation A-2) is written as:

$$\sigma_{eq}^h = \sigma_n \quad (\text{A-11})$$

where σ_n is the stress normal to the damage defined by:

$$\sigma_n = \frac{\sigma_1 + \sigma_3}{2} + \frac{\sigma_1 - \sigma_3}{2} \cos(2\theta) \quad (\text{A-12})$$

where:

σ_i = principal stresses ($i=1, 3$)

$$\theta = \frac{\pi}{2} - \alpha + d \quad (\text{A-13})$$

α = principal stress angle (+ccw from +x-axis).

d = damage angle (+ccw from +x-axis)

The principal stress angle can be defined in terms of the stress components in the plane and is written as:

$$\theta = \frac{1}{2} \tan^{-1} \left[\frac{2\sigma_{xy}}{\sigma_{xx} - \sigma_{yy}} \right] = \frac{1}{2} \tan^{-1} \left[\frac{2\sigma_{rz}}{\sigma_{rr} - \sigma_{zz}} \right] \quad (\text{A-14})$$

For two-dimensional planar and axisymmetric problems, the out-of-plane and tangential stresses are always principal stresses. Thus the above definition of the normal stress only holds true when the out-of-plane or tangential stress is the intermediate principal. Cases where the

¹ **Chan, K. S., 1996.** *Final Development of the Multimechanism Deformation Coupled Fracture (MDCF) Constitutive Model*, Monthly Technical Report No. FY '96-2, Monthly Progress Report for Southwest Research Institute, Contract AQ-1458 with Sandia National Laboratories, February.

out-of-plane or tangential principal stresses are the maximum or minimum principal stresses will be formulated following their consideration as the intermediate principal stress. From the above definition of normal stress, the flow potential for healing is written as:

$$\frac{\partial \sigma_{eq}^h}{\partial \sigma_{ij}} = \frac{\partial \sigma_n}{\partial \sigma_{ij}} = \frac{1}{2} \left\{ \frac{\partial (\sigma_1 + \sigma_3)}{\partial \sigma_{ij}} + \frac{\partial (\sigma_1 - \sigma_3)}{\partial \sigma_{ij}} \cos(2\theta) + (\sigma_1 - \sigma_3) \frac{\partial \cos(2\theta)}{\partial \sigma_{ij}} \right\} \quad (A-15)$$

Performing the indicated tensor differentiation produces:

$$\frac{\partial \sigma_{eq}^h}{\partial \sigma_{ij}} = \frac{1}{2} \left\{ \begin{aligned} & \frac{2\delta_{ij}}{3} + \frac{\sin(2\psi)}{\cos(3\psi)} \frac{s_{ij}}{\sqrt{3}J_2} + \frac{\cos(\psi)}{\cos(3\psi)} \frac{t_{ij}}{J_2} + \\ & \left[\frac{\cos(2\psi)}{\cos(3\psi)} \frac{s_{ij}}{\sqrt{J_2}} + \frac{\sqrt{3}\sin(\psi)}{\cos(3\psi)} \frac{t_{ij}}{J_2} \right] \cos(2\theta) + \tau_{ij} \end{aligned} \right\} \quad (A-16)$$

where:

$$\delta_{ij} = \begin{cases} 1 & \text{if } i=j \\ 0 & \text{if } i \neq j \end{cases} \quad (\text{Kronecker delta})$$

$$s_{ij} = \sigma_{ij} - \sigma_m \delta_{ij} \quad (\text{deviatoric stress})$$

$$\sigma_m = \frac{\sigma_{kk}}{3} \quad (\text{mean stress})$$

$$t_{ij} = s_{ik} s_{kj} - \frac{2}{3} J_2 \delta_{ij} \quad (\text{deviator of the square of the reduced stress})$$

$$\psi = \frac{1}{3} \sin^{-1} \left[\frac{-3}{2} \frac{\sqrt{3} J_3}{J_2^{3/2}} \right] \quad (\text{Lode angle})$$

$$J_2 = \frac{1}{2} s_{ij} s_{ji} \quad (2^{\text{nd}} \text{ invariant of stress deviator})$$

$$J_3 = \frac{1}{3} s_{ij} s_{jk} s_{ki} \quad (3^{\text{rd}} \text{ invariant of stress deviator}).$$

τ_{ij} represents the last term in the differential in Equation A-15 given by:

$$\tau_{ij} = (\sigma_1 - \sigma_3) \frac{\partial \cos(2\theta)}{\partial \sigma_{ij}} \quad (A-17)$$

with components defined by:

$$\begin{aligned}
\tau_{11} &= -\frac{\sin(2\theta)}{R}\sigma_{12} \\
\tau_{22} &= \frac{\sin(2\theta)}{R}\sigma_{12} \\
\tau_{12} &= \frac{\sin(2\theta)}{2R}(\sigma_{11} - \sigma_{22}) \\
\tau_{33} &= 0
\end{aligned} \tag{A-18}$$

where:

$$R = \left[\left(\frac{\sigma_{11} + \sigma_{22}}{2} \right)^2 + \sigma_{12}^2 \right]^{\frac{1}{2}} \tag{A-19}$$

The flow potential is seen to be undefined when the Lode angle is $\pm 30^\circ$. In other words, the flow potential forms corners for these values of the Lode angle. This occurs when two principal stress components are equal. If the two equal stress components are the major principal stress, a state of stress termed triaxial compression exists and the Lode angle is $+30^\circ$. If the two equal stress components are the minor principal stress, a state of stress termed triaxial extension exists and the Lode angle is -30° . At these corners, the direction of straining is not unique. To eliminate this problem computationally, the flow potentials on either side of the corner are averaged, which produces an indeterminate form that is examined in the limit as the Lode angle approaches $\pm 30^\circ$.

At the triaxial compression corner ($\psi = 30^\circ$), the average flow potential is written as:

$$\frac{\partial \sigma_{eq}^h}{\partial \sigma_{ij}} = \frac{1}{2} \left\{ \begin{aligned} & \left[\frac{2\delta_{ij}}{3} + \frac{\sin\left(2\psi - \frac{\pi}{3}\right)}{2\cos(3\psi)} \frac{s_{ij}}{\sqrt{3}J_2} + \frac{\cos\left(\psi + \frac{\pi}{3}\right)}{2\cos(3\psi)} \frac{t_{ij}}{J_2} - \right. \\ & \left. \left[\frac{\sqrt{3}\sin\left(2\psi - \frac{\pi}{3}\right)}{2\cos(3\psi)} \frac{s_{ij}}{\sqrt{J_2}} + \frac{3\cos\left(\psi + \frac{\pi}{3}\right)}{2\cos(3\psi)} \frac{t_{ij}}{J_2} \right] \cos(2\theta) + \tau_{ij} \right] \end{aligned} \right\} \tag{A-20}$$

Examining the limit as $\psi \rightarrow 30^\circ$, yields the flow potential at the triaxial compression corner:

$$\lim_{\psi \rightarrow \frac{\pi}{6}} \frac{\partial \sigma_{eq}^h}{\partial \sigma_{ij}} = \frac{1}{2} \left\{ \frac{2\delta_{ij}}{3} + \left[\cos(2\theta) - \frac{1}{3} \right] \left(\frac{s_{ij}}{\sqrt{3}J_2} - \frac{t_{ij}}{2J_2} \right) + \tau_{ij} \right\} \tag{A-21}$$

At the triaxial extension corner ($\psi = -30^\circ$), the average flow potential is written as:

$$\frac{\partial \sigma_{eq}^h}{\partial \sigma_{ij}} = \frac{1}{2} \left\{ \begin{array}{l} \frac{2\delta_{ij}}{3} + \frac{\cos\left(2\psi - \frac{\pi}{6}\right)}{2\cos(3\psi)} \frac{s_{ij}}{\sqrt{3J_2}} + \frac{\sin\left(\psi + \frac{\pi}{6}\right)}{2\cos(3\psi)} \frac{t_{ij}}{J_2} + \\ \left[\frac{\sqrt{3}\cos\left(2\psi - \frac{\pi}{6}\right)}{2\cos(3\psi)} \frac{s_{ij}}{\sqrt{J_2}} + \frac{3\sin\left(\psi + \frac{\pi}{6}\right)}{2\cos(3\psi)} \frac{t_{ij}}{J_2} \right] \cos(2\theta) + \tau_{ij} \end{array} \right\} \quad (\text{A-22})$$

Examining the limit as $\psi \rightarrow -30^\circ$, yields the flow potential at the triaxial extension corner:

$$\frac{\partial \sigma_{eq}^h}{\partial \sigma_{ij}} = \frac{1}{2} \left\{ \frac{2\delta_{ij}}{3} + \left[\cos(2\theta) + \frac{1}{3} \right] \left(\frac{s_{ij}}{\sqrt{3J_2}} + \frac{t_{ij}}{2J_2} \right) + \tau_{ij} \right\} \quad (\text{A-23})$$

$\lim_{\psi \rightarrow -\frac{\pi}{6}}$

If the out-of-plane or tangential stress in two-dimensional planar or axisymmetric problems is the maximum principal stress (i.e., σ_1), the flow potential is written in terms of the in-plane principal stresses as:

$$\frac{\partial \sigma_{eq}^h}{\partial \sigma_{ij}} = \frac{\partial \sigma_n}{\partial \sigma_{ij}} = \frac{1}{2} \left\{ \frac{\partial(\sigma_2 + \sigma_3)}{\partial \sigma_{ij}} + \frac{\partial(\sigma_2 - \sigma_3)}{\partial \sigma_{ij}} \cos(2\theta) + (\sigma_2 - \sigma_3) \frac{\partial \cos(2\theta)}{\partial \sigma_{ij}} \right\} \quad (\text{A-24})$$

Performing the indicated tensor differentiation produces:

$$\frac{\partial \sigma_{eq}^h}{\partial \sigma_{ij}} = \frac{1}{2} \left\{ \begin{array}{l} \frac{2\delta_{ij}}{3} + \frac{\sin\left(2\psi - \frac{2\pi}{3}\right)}{\cos(3\psi)} \frac{s_{ij}}{\sqrt{3J_2}} + \frac{\cos\left(\psi + \frac{2\pi}{3}\right)}{\cos(3\psi)} \frac{t_{ij}}{J_2} - \\ \left[\frac{\cos\left(2\psi - \frac{2\pi}{3}\right)}{\cos(3\psi)} \frac{s_{ij}}{\sqrt{J_2}} + \frac{\sqrt{3}\sin\left(\psi + \frac{2\pi}{3}\right)}{\cos(3\psi)} \frac{t_{ij}}{J_2} \right] \cos(2\theta) + \tau_{ij} \end{array} \right\} \quad (\text{A-25})$$

Again, the corners in the flow potential need to be evaluated. At the triaxial compression corner ($\psi = 30^\circ$), the average flow potential is written as:

$$\frac{\partial \sigma_{eq}^h}{\partial \sigma_{ij}} = \frac{1}{2} \left\{ \left[\frac{2\delta_{ij}}{3} + \frac{\sin\left(2\psi - \frac{\pi}{3}\right)}{2\cos(3\psi)} \frac{s_{ij}}{\sqrt{3}J_2} + \frac{\cos\left(\psi + \frac{\pi}{3}\right)}{2\cos(3\psi)} \frac{t_{ij}}{J_2} - \frac{\sqrt{3}\sin\left(2\psi - \frac{\pi}{3}\right)}{2\cos(3\psi)} \frac{s_{ij}}{\sqrt{J_2}} + \frac{3\cos\left(\psi + \frac{\pi}{3}\right)}{2\cos(3\psi)} \frac{t_{ij}}{J_2} \right] \cos(2\theta) + \tau_{ij} \right\} \quad (\text{A-26})$$

Examining the limit as $\psi \rightarrow 30^\circ$, yields the flow potential at the triaxial compression corner:

$$\lim_{\psi \rightarrow \frac{\pi}{6}} \frac{\partial \sigma_{eq}^h}{\partial \sigma_{ij}} = \frac{1}{2} \left\{ \frac{2\delta_{ij}}{3} + \left[\cos(2\theta) - \frac{1}{3} \right] \left(\frac{s_{ij}}{\sqrt{3}J_2} - \frac{t_{ij}}{2J_2} \right) + \tau_{ij} \right\} \quad (\text{A-27})$$

At the triaxial extension corner ($\psi = -30^\circ$), the average flow potential is written as:

$$\frac{\partial \sigma_{eq}^h}{\partial \sigma_{ij}} = \frac{1}{2} \left\{ \frac{2\delta_{ij}}{3} + \frac{\sin\left(2\psi - \frac{2\pi}{3}\right)}{\cos(3\psi)} \frac{s_{ij}}{\sqrt{3}J_2} + \frac{\cos\left(\psi + \frac{2\pi}{3}\right)}{\cos(3\psi)} \frac{t_{ij}}{J_2} + \tau_{ij} \right\} \quad (\text{A-28})$$

Examining the limit as $\psi \rightarrow -30^\circ$, yields the flow potential at the triaxial extension corner:

$$\lim_{\psi \rightarrow -\frac{\pi}{6}} \frac{\partial \sigma_{eq}^h}{\partial \sigma_{ij}} = \frac{1}{3} \left\{ \delta_{ij} - \frac{s_{ij}}{\sqrt{3}J_2} - \frac{t_{ij}}{2J_2} \right\} + \frac{\tau_{ij}}{2} \quad (\text{A-29})$$

If the out-of-plane or tangential stress in two-dimensional planar or axisymmetric problems is the minimum principal stress (i.e., σ_3), the flow potential is written in terms of the in-plane principal stresses as:

$$\frac{\partial \sigma_{eq}^h}{\partial \sigma_{ij}} = \frac{\partial \sigma_n}{\partial \sigma_{ij}} = \frac{1}{2} \left\{ \frac{\partial(\sigma_1 + \sigma_2)}{\partial \sigma_{ij}} + \frac{\partial(\sigma_1 - \sigma_2)}{\partial \sigma_{ij}} \cos(2\theta) + (\sigma_1 - \sigma_2) \frac{\partial \cos(2\theta)}{\partial \sigma_{ij}} \right\} \quad (\text{A-30})$$

Performing the indicated tensor differentiation produces:

$$\frac{\partial \sigma_{eq}^h}{\partial \sigma_{ij}} = \frac{1}{2} \left\{ \begin{array}{l} \frac{2\delta_{ij}}{3} - \frac{\sin\left(2\psi - \frac{\pi}{3}\right)}{\cos(3\psi)} \frac{s_{ij}}{\sqrt{3J_2}} - \frac{\cos\left(\psi + \frac{\pi}{3}\right)}{\cos(3\psi)} \frac{t_{ij}}{J_2} + \\ \left[\frac{\cos\left(2\psi - \frac{\pi}{3}\right)}{\cos(3\psi)} \frac{s_{ij}}{\sqrt{J_2}} + \frac{\sqrt{3}\sin\left(\psi + \frac{\pi}{3}\right)}{\cos(3\psi)} \frac{t_{ij}}{J_2} \right] \cos(2\theta) + \tau_{ij} \end{array} \right\} \quad (\text{A-31})$$

Again, the corners in the flow potential need to be evaluated. At the triaxial compression corner ($\psi = 30^\circ$), the average flow potential is written as:

$$\frac{\partial \sigma_{eq}^h}{\partial \sigma_{ij}} = \frac{1}{2} \left\{ \frac{2\delta_{ij}}{3} - \frac{\sin\left(2\psi - \frac{\pi}{3}\right)}{\cos(3\psi)} \frac{s_{ij}}{\sqrt{3J_2}} - \frac{\cos\left(\psi + \frac{\pi}{3}\right)}{\cos(3\psi)} \frac{t_{ij}}{J_2} + \tau_{ij} \right\} \quad (\text{A-32})$$

Examining the limit as $\psi \rightarrow 30^\circ$, yields the flow potential at the triaxial compression corner:

$$\lim_{\psi \rightarrow \frac{\pi}{6}} \frac{\partial \sigma_{eq}^h}{\partial \sigma_{ij}} = \frac{1}{3} \left\{ \delta_{ij} + \frac{s_{ij}}{\sqrt{3J_2}} - \frac{t_{ij}}{2J_2} \right\} + \frac{\tau_{ij}}{2} \quad (\text{A-33})$$

At the triaxial extension corner ($\psi = -30^\circ$), the average flow potential is written as:

$$\frac{\partial \sigma_{eq}^h}{\partial \sigma_{ij}} = \frac{1}{2} \left\{ \begin{array}{l} \frac{2\delta_{ij}}{3} + \frac{\cos\left(2\psi - \frac{\pi}{6}\right)}{2\cos(3\psi)} \frac{s_{ij}}{\sqrt{3J_2}} + \frac{\sin\left(\psi + \frac{\pi}{6}\right)}{2\cos(3\psi)} \frac{t_{ij}}{J_2} + \\ \left[\frac{\sqrt{3}s\cos\left(2\psi - \frac{\pi}{6}\right)}{2\cos(3\psi)} \frac{s_{ij}}{\sqrt{J_2}} + \frac{3\sin\left(\psi + \frac{\pi}{6}\right)}{2\cos(3\psi)} \frac{t_{ij}}{J_2} \right] \cos(2\theta) + \tau_{ij} \end{array} \right\} \quad (\text{A-34})$$

Examining the limit as $\psi \rightarrow -30^\circ$, yields the flow potential at the triaxial extension corner:

$$\lim_{\psi \rightarrow -\frac{\pi}{6}} \frac{\partial \sigma_{eq}^h}{\partial \sigma_{ij}} = \frac{1}{2} \left\{ \frac{2\delta_{ij}}{3} + \left[\cos(2\theta) + \frac{1}{3} \right] \left(\frac{s_{ij}}{\sqrt{3J_2}} + \frac{t_{ij}}{2J_2} \right) + \tau_{ij} \right\} \quad (\text{A-35})$$

A.2 REDUCTION TO TRIAXIAL COMPRESSION AND TRIAXIAL EXTENSION TESTS

For testing and observational purposes, it is useful to reduce the equations for healing to their simplest form under triaxial compression and triaxial extension test conditions. This work is partially accomplished in the previous section because of the indeterminacy encountered when two principal stresses are equal. Recall that the indeterminacies were evaluated in the limit as the Lode angle approaches $\pm 30^\circ$. The equations presented in the previous section may be further simplified by substituting the numerical value of the stress invariants encountered for triaxial compression and triaxial extension. These values are:

Triaxial Compression Test

$$\begin{aligned}
 \sqrt{3J_2} &= \Delta\sigma = \sigma_1 - \sigma_3 \\
 J_2 &= \frac{\Delta\sigma^2}{3} \\
 s_{11} = s_{22} &= \sigma_{11} - \sigma_m = \frac{\Delta\sigma}{3} \\
 s_{33} &= \sigma_{33} - \sigma_m = -\frac{2}{3}\Delta\sigma \\
 t_{11} = t_{22} &= s_{11}^2 + s_{12}^2 - \frac{2}{3}J_2 = -\frac{\Delta\sigma^2}{9} \\
 t_{33} &= s_{33}^2 - \frac{2}{3}J_2 = \frac{2}{9}\Delta\sigma^2 \\
 \left(\frac{s_{11}}{\sqrt{3J_2}} - \frac{t_{11}}{2J_2} \right) &= \left(\frac{s_{22}}{\sqrt{3J_2}} - \frac{t_{22}}{2J_2} \right) = \frac{1}{2} \\
 \left(\frac{s_{33}}{\sqrt{3J_2}} - \frac{t_{33}}{2J_2} \right) &= -1
 \end{aligned} \tag{A-36}$$

Triaxial Extension Test

$$\begin{aligned}
 \sqrt{3J_2} &= \Delta\sigma = \sigma_1 - \sigma_3 \\
 J_2 &= \frac{\Delta\sigma^2}{3} \\
 s_{11} = s_{22} &= \sigma_{11} - \sigma_m = -\frac{\Delta\sigma}{3} \\
 s_{33} &= \sigma_{33} - \sigma_m = \frac{2}{3}\Delta\sigma \\
 t_{11} = t_{22} &= s_{11}^2 + s_{12}^2 - \frac{2}{3}J_2 = -\frac{\Delta\sigma^2}{9}
 \end{aligned} \tag{A-37}$$

$$t_{33} = s_{33}^2 - \frac{2}{3} J_2 = \frac{2 \Delta \sigma^2}{9}$$

$$\left(\frac{s_{11}}{\sqrt{3} J_2} + \frac{t_{11}}{2 J_2} \right) = \left(\frac{s_{22}}{\sqrt{3} J_2} + \frac{t_{22}}{2 J_2} \right) = -\frac{1}{2}$$

$$\left(\frac{s_{33}}{\sqrt{3} J_2} + \frac{t_{33}}{2 J_2} \right) = 1$$

Substituting Equations A-36 and A-37 into Equations A-21 and A-23 (out-of-plane or tangential stress is the intermediate principal stress), Equations A-27 and A-29 (out-of-plane or tangential stress is major principal stress), and Equations A-33 and A-35 (out-of-plane or tangential stress is the minor principal stress) with the result substituted into Equation A-2, produces the strain rate for triaxial compression and extension tests. Performing the indicated operation and using subscripts a , l , and v for the axial, lateral, and volumetric components, respectively, produces:

Out-of-Plane or Tangential Stress is the Intermediate Principal Stress

In a triaxial compression test, $\theta = \pi$ so that the strain rates would be:

$$\dot{\epsilon}_a^h = \dot{\epsilon}_{eq}^h \frac{1}{2} (1 - \cos 2\theta) = 0$$

$$\dot{\epsilon}_l^h = \dot{\epsilon}_{eq}^h \frac{1}{4} (1 + \cos 2\theta) = \frac{\dot{\epsilon}_{eq}^h}{2} \quad (\text{A-38})$$

$$\dot{\epsilon}_v^h = \dot{\epsilon}_{eq}^h$$

In a triaxial extension test, $\theta = 0$ so that the strain rates would be:

$$\dot{\epsilon}_a^h = \dot{\epsilon}_{eq}^h \frac{1}{2} (1 + \cos 2\theta) = \dot{\epsilon}_{eq}^h$$

$$\dot{\epsilon}_l^h = \dot{\epsilon}_{eq}^h \frac{1}{4} (1 - \cos 2\theta) = 0 \quad (\text{A-39})$$

$$\dot{\epsilon}_v^h = \dot{\epsilon}_{eq}^h$$

Note that under both triaxial compression and triaxial extension conditions, $\tau_{ij} = 0$.

Out-of-Plane or Tangential Stress is the Maximum Principal Stress

In a triaxial compression test, $\theta = \pi$ so that the strain rates would be:

$$\begin{aligned}\dot{\epsilon}_a^h &= \dot{\epsilon}_{eq}^h \frac{1}{2}(1 - \cos 2\theta) = 0 \\ \dot{\epsilon}_l^h &= \dot{\epsilon}_{eq}^h \frac{1}{4}(1 + \cos 2\theta) = \frac{\dot{\epsilon}_{eq}^h}{2} \\ \dot{\epsilon}_v^h &= \dot{\epsilon}_{eq}^h\end{aligned}\tag{A-40}$$

In a triaxial extension test, $\theta = 0$ so that the strain rates would be:

$$\begin{aligned}\dot{\epsilon}_a^h &= \dot{\epsilon}_{eq}^h \frac{1}{3}(1 - 1) = 0 \\ \dot{\epsilon}_l^h &= \dot{\epsilon}_{eq}^h \frac{1}{3} \left(1 - \left(-\frac{1}{2} \right) \right) = \frac{\dot{\epsilon}_{eq}^h}{2} \\ \dot{\epsilon}_v^h &= \dot{\epsilon}_{eq}^h\end{aligned}\tag{A-41}$$

Out-of-Plane or Tangential Stress is the Minimum Principal Stress

In a triaxial compression test, $\theta = \pi$ so that the strain rates would be:

$$\begin{aligned}\dot{\epsilon}_a^h &= \dot{\epsilon}_{eq}^h \frac{1}{3}(1 - 1) = 0 \\ \dot{\epsilon}_l^h &= \dot{\epsilon}_{eq}^h \frac{1}{3} \left(1 + \frac{1}{2} \right) = \frac{\dot{\epsilon}_{eq}^h}{2} \\ \dot{\epsilon}_v^h &= \dot{\epsilon}_{eq}^h\end{aligned}\tag{A-42}$$

Note that the case given in Equation A-42 is impossible for axisymmetric geometry. This is true because the tangential stress is equal to the radial stress. In triaxial compression, the axial stress is the minimum principal stress. Thus if the tangential stress were the minimum principal stress, then a state of hydrostatic compression would have to exist. In a triaxial extension test, $\theta = 0$ so that the strain rates would be:

$$\begin{aligned}\dot{\epsilon}_a^h &= \dot{\epsilon}_{eq}^h \frac{1}{2}(1 + \cos 2\theta) = \dot{\epsilon}_{eq}^h \\ \dot{\epsilon}_l^h &= \dot{\epsilon}_{eq}^h \frac{1}{4}(1 - \cos 2\theta) = 0 \\ \dot{\epsilon}_v^h &= \dot{\epsilon}_{eq}^h\end{aligned}\tag{A-43}$$

APPENDIX B

POTENTIAL MODIFICATION TO THE POWER-CONJUGATE EQUIVALENT STRESS MEASURES FOR SHEAR-INDUCED DAMAGE

APPENDIX B

POTENTIAL MODIFICATION TO THE POWER-CONJUGATE EQUIVALENT STRESS MEASURES FOR SHEAR-INDUCED DAMAGE

The MDCF model uses two different power-conjugate equivalent stress measures for shear-induced damage. One is power-conjugate equivalent stress measure used to describe the inelastic shear-induced damage equivalent strain rate. The other is the associated power-conjugate stress measure used to describe the flow potential (hereafter called simply the equivalent stress measure and flow potential). Before discussing modifications to the power-conjugate equivalent stress measures for shear-induced damage, it is important to examine general states of stress and show the inability of the equivalent stress measure and flow potential, as they are currently defined, to represent the expected behavior at general states of stress. The equivalent stress measure ($\sigma_{eq}^{\omega_s}$) and flow potential stress ($\sigma_{eq}^{\omega_s^*}$) for shear-induced damage are currently defined as:

$$\sigma_{eq}^{\omega_s} = |\sigma_1 - \sigma_3| + f_p x_2 x_7 \operatorname{sgn}(I_1 - \sigma_3) \left(\frac{I_1 - \sigma_3}{3 x_7 \operatorname{sgn}(I_1 - \sigma_3)} \right)^{x_6} \quad (\text{B-1})$$

$$\sigma_{eq}^{\omega_s^*} = |\sigma_1 - \sigma_3| + \frac{x_2 x_8}{3} (I_1 - \sigma_3)$$

where:

σ_i = principal stresses ($i = 1, 2, 3$)

I_1 = first stress invariant = $\sigma_1 + \sigma_2 + \sigma_3$

f_p = material parameter related to impurity content = $1 - \rho_1 \rho$

$x_2, x_6, x_7, x_8, \rho_1$ = material constants

ρ = impurity content

$\operatorname{sgn}(\bullet)$ = sign of the argument.

Development of Equation B-1 was guided by laboratory test data collected predominately from triaxial compression tests ($\sigma_1 = \sigma_2 > \sigma_3$) as illustrated in Figure B-1 (tension is assumed to be positive). The different equivalent stress measure and flow potential stress provide for a nonassociative type of formulation that provides greater flexibility in the ability to predict the volumetric behavior. In a triaxial compression test, the magnitude of the compressive confining pressure is less than the magnitude of the compressive axial stress. Figure B-1 also illustrates the triaxial extension test ($\sigma_1 > \sigma_2 = \sigma_3$) where the magnitude of the compressive confining pressure is greater than the magnitude of the compressive axial stress. While these two types

of tests do not look substantially different, the results from these two types of tests can be dramatically different if the behavior of the material being tested depends on the intermediate principal stress. Most rocks behave differently in triaxial compression and extension with the material being weaker in extension. Fortunately, the generalized Mohr-Coulomb criterion captures this difference in material behavior.

RSI-1153-01-017

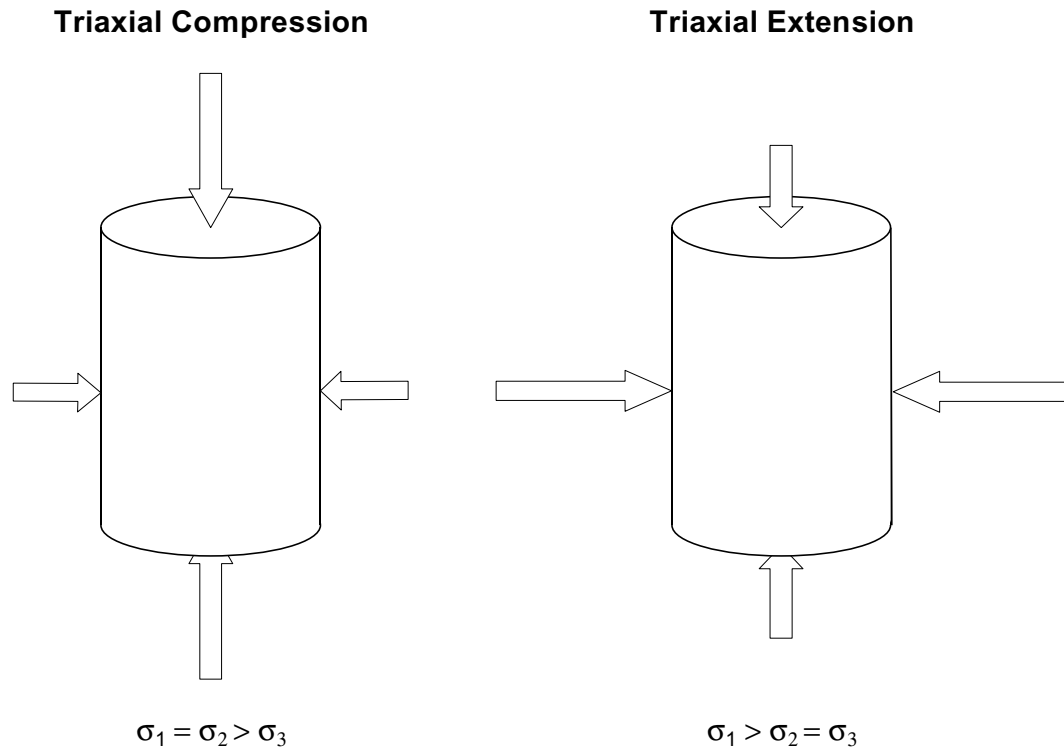


Figure B-1. Illustration of Triaxial Compression and Triaxial Extension Tests Performed on Circular Cylindrical Specimens.

The next section discusses the representation of states of stress in principal stress space, which will aid our examination of the existing equivalent stress measure and flow potential stress and help guide the development of alternative functional forms.

B.1 REPRESENTATION OF STATES OF STRESS IN PRINCIPAL STRESS SPACE

The representation of states of stress in principal-stress space is considered to help facilitate the discussion of states of stress around underground caverns and as a means to visualize those states of stress. Consider the state of stress at a point (Q) in a body represented by the principal stresses σ_i ($i = 1, 2, 3$) at that point as shown in Figure B-2. If the principal stresses

are taken as the Cartesian coordinates in a three-dimensional space, an isotropic potential (or yield) surface may be mapped in the coordinate system. A vivid two-dimensional illustration of the bounding states of stress is achieved by projecting these stresses into the π -plane or Haigh-Westergaard stress space (e.g., Chen and Han [1988]). The π -plane is a plane perpendicular the hydrostatic axis ($\sigma_1 = \sigma_2 = \sigma_3$) where the mean stress ($\sigma_m = (\sigma_1 + \sigma_2 + \sigma_3)/3$) is zero, and Haigh-Westergaard stress space is similar to the π -plane but includes those planes where the mean stress is a nonzero constant. For simplicity, these representations will be referred to as the π -plane recognizing the shortcomings in nomenclature as stated above. Local two-dimensional Cartesian and polar coordinate systems embedded in the π -plane are convenient for representing yield or potential surfaces. This fact exists because a unique state of stress can also be uniquely defined by three stress invariants, and yield and potential functions are typically written in terms of stress invariants. Of particular interest are the invariants of the deviatoric stress tensor, S_{ij} ($S_{ij} = \sigma_{ij} - \sigma_m \delta_{ij}$), which are:

$$\begin{aligned} J_1 &= 0 \\ J_2 &= \frac{1}{2} S_{ij} S_{ji} \\ J_3 &= \frac{1}{3} S_{ij} S_{jk} S_{ki} \end{aligned} \quad (\text{B-2})$$

Now consider the principal stress space of Figure B-3. Figure B-3 is a view looking directly down the hydrostatic axis. In this orientation, the principal stress coordinate axes appear to be 120° apart. Cartesian coordinates x and y are defined as shown in Figure B-3 (the choice is arbitrary). The x and y axes selected originate at point O on the hydrostatic axis. The x -axis is located 30° counter-clockwise from the σ_1 -axis, and the y -axis lies along (but not parallel to) the σ_2 -axis. In terms of the principal stresses, the coordinates are:

$$x = \frac{\sigma_1 - \sigma_3}{\sqrt{2}} \quad (\text{B-3})$$

$$y = \frac{2\sigma_2 - \sigma_1 - \sigma_3}{\sqrt{6}} \quad (\text{B-4})$$

Equations B-3 and B-4 may be used to obtain a polar coordinate (r, ψ) system; viz,

$$r = \sqrt{x^2 + y^2} = \frac{1}{\sqrt{3}} \sqrt{(\sigma_1 - \sigma_2)^2 + (\sigma_2 - \sigma_3)^2 + (\sigma_3 - \sigma_1)^2} \quad (\text{B-5})$$

$$\psi = \tan^{-1} \left(\frac{y}{x} \right) = \tan^{-1} \frac{1}{\sqrt{3}} \left[\frac{2\sigma_2 - \sigma_1 - \sigma_3}{\sigma_1 - \sigma_3} \right] \quad (\text{B-6})$$

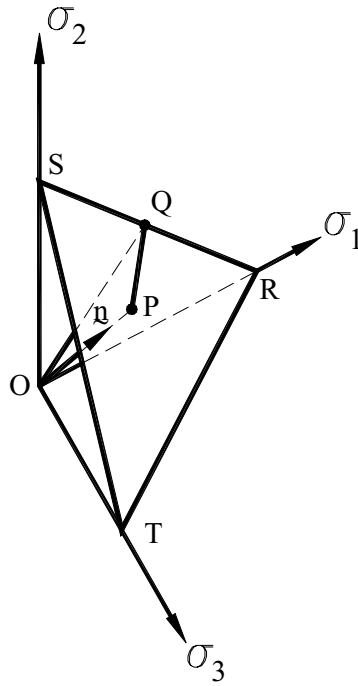


Figure B-2. Stress Points in Principal Stress Space.

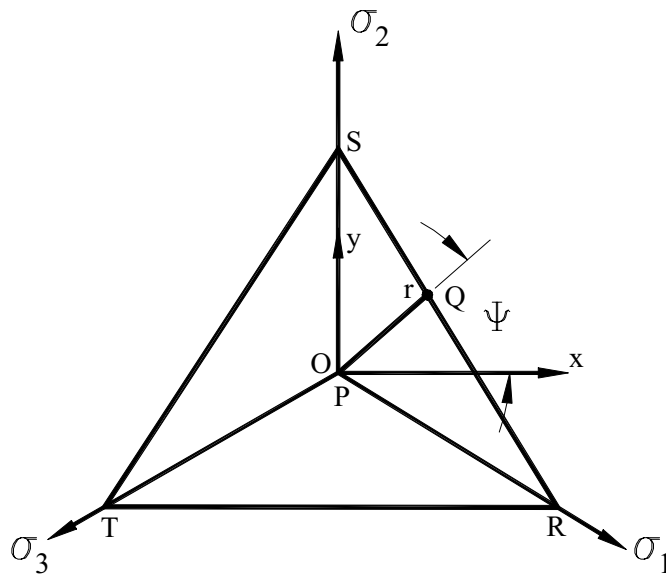


Figure B-3. Stress Points in Principal Stress Space Viewed Down the Hydrostatic Axis.

The angle ψ is referred to as the Lode angle. The Lode angle may be expressed in terms of the invariants J_2 and J_3 as [Nayak and Zienkiewicz, 1972]:

$$\psi = \frac{1}{3} \sin^{-1} \left[\frac{-3\sqrt{3}J_3}{2J_2^{3/2}} \right] \quad (\text{B-7})$$

However, when the Lode angle is defined in this manner, it is restricted to $-30^\circ \leq \psi \leq 30^\circ$. This restriction requires symmetry of the yield condition in all 60° sextants in the π -plane. When J_2 is expressed in terms of the principal stresses, it becomes:

$$J_2 = \frac{1}{6} \{ (\sigma_1 - \sigma_2)^2 + (\sigma_2 - \sigma_3)^2 + (\sigma_1 - \sigma_3)^2 \} \quad (\text{B-8})$$

From Equations B-5 and B-8, one readily sees that the distance from the hydrostatic axes to a stress point is equivalent to $\sqrt{2J_2}$ when lying in the π -plane. Potential or yield functions expressed in terms of these coordinate systems may be plotted in the π -plane easily. Figure B-4 illustrates the Mohr-Coulomb criterion plotted in the π -plane using these coordinate systems. Stress lines of interest (triaxial compression ($\psi = \pi/6$) and extension ($\psi = -\pi/6$) are labeled along with the ordering of the principal stresses in the sextants.

Using this information, the flow potential equivalent stress presently defined for the MDCF model (Equation B-1) can be plotted in principal stress space as shown in Figure B-5. Figure B-5 reveals that the present flow potential equivalent stress actually describes a material that is stronger in triaxial extension than in triaxial compression, which is contrary to available information on the behavior of rock. This could be surmised by observing the role that the $I_1 - \sigma_3$ term plays in the definition of the stress measure in Equation B-1. Damage occurs when the effective stress measure is positive. Thus the $I_1 - \sigma_3$ term represents the stresses or confinement that suppresses damage. In a triaxial compression test (Figure B-1), $I_1 - \sigma_3$ represents the confining pressure in the test, which suppresses the microfracturing generated parallel to the axial direction in the test specimen. However, in a triaxial extension test where the microfractures would be generated perpendicular to the axial direction, the $I_1 - \sigma_3$ term is not indicative of the axial stress (the major principal stress (σ_1) in a triaxial extension test). The $I_1 - \sigma_3 = \sigma_1 + \sigma_2$ term obviously overestimates the magnitude of the stresses suppressing damage for a triaxial extension state of stress making the material seem stronger than it actually is. Unfortunately, the functional form also makes the material appear to be stronger at all states of stress between triaxial compression and extension. To remedy this problem, new Mohr-Coulomb type functional forms are developed in the next section that makes the material weaker in extension.

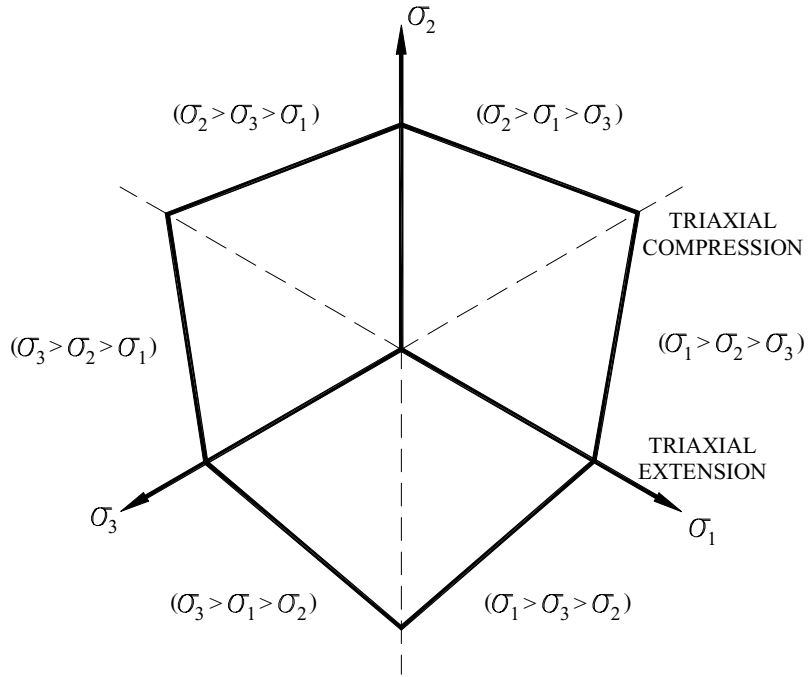


Figure B-4. Mohr-Coulomb Yield Surface in Principal Stress Space.

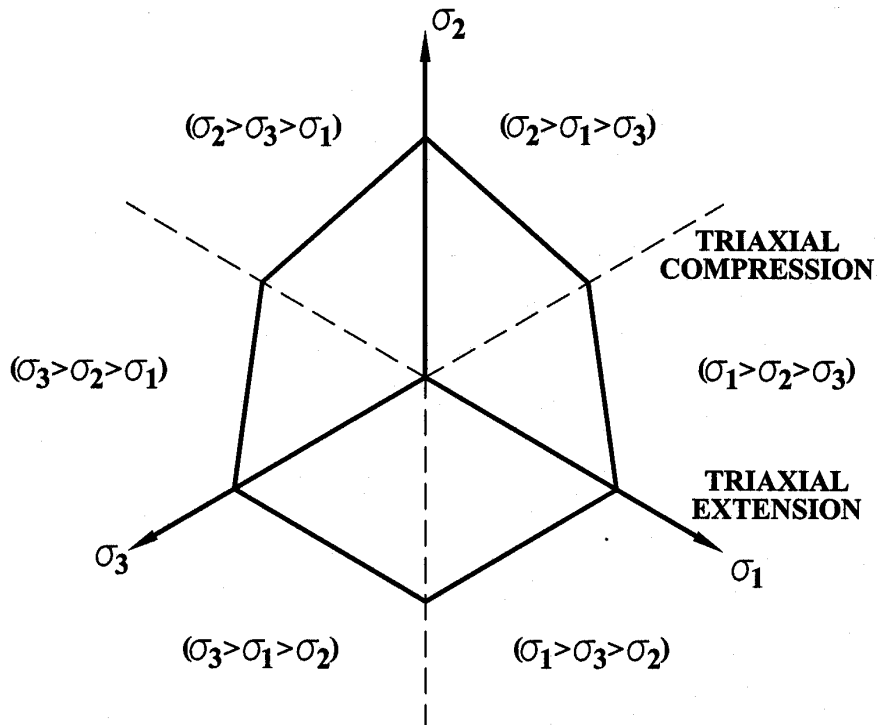


Figure B-5. Multimechanism Deformation Coupled Fracture Flow Potential Function Plotted in Principal Stress Space.

B.2 ALTERNATE DAMAGE EFFECTIVE STRESS AND FLOW POTENTIAL

The damage effective stress and flow potential presently defined in the MDCF model are given in Equation 1. The objective of this section is to describe new functional forms that remove the deficiencies inherent in the current forms used in the MDCF model. To accomplish this task, alternative damage effective stress and flow potentials are developed based on the Mohr-Coulomb criterion. The Mohr-Coulomb criterion is typically written in its familiar linear form as:

$$|\tau| = S_0 - \sigma_n \tan \phi \quad (\text{B-9})$$

where τ is the shear stress along the failure plane, σ_n is the normal stress on the plane, ϕ is the angle of internal friction, and S_0 is the material cohesion. The shear and normal stresses are written as:

$$\begin{aligned} \sigma_n &= \frac{\sigma_1 + \sigma_3}{2} + \frac{\sigma_1 - \sigma_3}{2} \cos(2\gamma) \\ |\tau| &= \left| \frac{\sigma_1 - \sigma_3}{2} \sin(2\gamma) \right| \\ \gamma &= \frac{\pi}{4} + \frac{\phi}{2} \end{aligned} \quad (\text{B-10})$$

After substitution of Equations B-10 into Equation B-9 and rearrangement, Equation B-9 may be written as:

$$\frac{\sigma_1 - \sigma_3}{2} = S_0 \cos(\phi) - \frac{\sigma_1 + \sigma_3}{2} \sin(\phi) \quad (\text{B-11})$$

and restated as:

$$\sigma_1 - \sigma_3 = 2 S_0 \cos(\phi) - (\sigma_1 + \sigma_3) \sin(\phi) \quad (\text{B-12})$$

When the Mohr-Coulomb criterion is written in invariant form using the invariants σ_m , J_2 , and ψ , it becomes (e.g., Callahan [1982]):

$$2\sqrt{J_2} \left(\cos \psi - \frac{1}{\sqrt{3}} \sin \psi \sin \phi \right) + 2\sigma_m \sin \phi - 2S_0 \cos \phi = 0 \quad (\text{B-13})$$

When plotted in principal stress space, Equation B-13 reproduces Figure B-4. Thus adoption of functional forms similar to Equation B-13 will produce the desired weaker material in triaxial extension and remove the deficiencies inherent in the current functional forms of the effective stress measure and flow potential. Therefore, suggested functional forms for the damage effective stress and flow potential are:

$$\begin{aligned}\sigma_{eq}^{\omega_s} &= 2 \sqrt{J_2} (\cos \psi - \eta \sin \psi) + 2\sqrt{3} \eta \sigma_m - C \\ \sigma_{eq}^{\omega_s^*} &= 2 \sqrt{J_2} (\cos \psi - \kappa \sin \psi) + 2\sqrt{3} \kappa \sigma_m\end{aligned}\tag{B-14}$$

where η and κ are material constants to be determined through laboratory testing. Once test data is available, especially triaxial extension test data, the functional forms and material constants may require modification. For example, the influence of impurities and the nonlinear dependence on mean stress could be included much like the present functional forms given in Equation B-1.

The shear-induced damage strain rate ($\dot{\epsilon}_{ij}^{\omega_s}$) is written in terms of the power-conjugate equivalent stress measures as:

$$\dot{\epsilon}_{ij}^{\omega_s} = \dot{\epsilon}_{eq}^{\omega_s} \frac{\partial \sigma_{eq}^{\omega_s^*}}{\partial \sigma_{ij}}\tag{B-15}$$

where the equivalent inelastic shear-induced damage strain rate ($\dot{\epsilon}_{eq}^{\omega_s}$) definition has not changed, but the shear-induced damage effective stress ($\sigma_{eq}^{\omega_s}$ given in Equation B-14) that it depends upon has changed. The shear-induced flow potential is:

$$\begin{aligned}\frac{\partial \sigma_{eq}^{\omega_s^*}}{\partial \sigma_{ij}} &= 2\kappa \frac{\delta_{ij}}{\sqrt{3}} + (\cos(2\psi) + \kappa \sin(2\psi)) \frac{S_{ij}}{2\sqrt{J_2} \cos(3\psi)} \\ &\quad - \sqrt{J_2} (\sin(\psi) + \kappa \cos(\psi)) \frac{\tan(3\psi)}{3J_3} t_{ij}\end{aligned}\tag{B-16}$$

where:

$$t_{ij} = S_{ip} S_{pj} - \frac{2}{3} J_2 \delta_{ij}$$

Reviewing the flow potential given in Equation B-16, one observes an indeterminacy when the intermediate principal stress is equal to either the maximum or minimum principal stress (i.e., triaxial compression and extension states of stress). In other words, a unique strain rate direction cannot be determined. Under these conditions, the Lode angle (ψ) is equal to $\pm \pi/6$. To eliminate this problem computationally, the flow potential is taken as the average of the flow potentials on either side of the corner and evaluated in the limit as $\psi \rightarrow \pm \pi/6$. Performing this limiting operation as $\psi \rightarrow \pm \pi/6$ (the triaxial compression corner), Equation B-16 becomes:

$$\frac{\partial \sigma_{eq}^{\omega_s^*}}{\partial \sigma_{ij}} = 2\kappa \frac{\delta_{ij}}{\sqrt{3}} + \frac{\sqrt{3} - \kappa}{6} \left[\frac{S_{ij}}{\sqrt{3}J_2} + \frac{\sqrt{J_2}}{3\sqrt{3}J_3} t_{ij} \right]\tag{B-17}$$

Equation B-17 may be further reduced for the triaxial compression conditions (i.e., $\sigma_1 > \sigma_2 = \sigma_3$) and substituted into Equation B-15 to yield the individual strain rate components; viz,

$$\begin{aligned}\dot{\epsilon}_{11}^{\omega_s} &= \dot{\epsilon}_{22}^{\omega_s} = \dot{\epsilon}_{eq}^{\omega_s} \left(\frac{2\kappa}{\sqrt{3}} + \frac{3+\kappa}{12} \right) \\ \dot{\epsilon}_{33}^{\omega_s} &= \dot{\epsilon}_{eq}^{\omega_s} \left(\frac{2\kappa}{\sqrt{3}} - \frac{3+\kappa}{6} \right) \\ \dot{\epsilon}_v^{\omega_s} &= 2\sqrt{3} \kappa \dot{\epsilon}_{eq}^{\omega_s}\end{aligned}\tag{B-18}$$

Similarly, performing this limiting operation as $\psi \rightarrow -\pi/6$ (the triaxial extension corner), Equation B-16 becomes:

$$\frac{\partial \sigma_{eq}^{\omega_s}}{\partial \sigma_{ij}} = 2\kappa \frac{\delta_{ij}}{\sqrt{3}} + \frac{\sqrt{3} + \kappa}{6} \left[\frac{S_{ij}}{\sqrt{3}J_2} + \frac{\sqrt{J_2} t_{ij}}{3\sqrt{3}J_3} \right]\tag{B-19}$$

Equation B-19 may be further reduced for the triaxial extension conditions (i.e., $\sigma_1 = \sigma_2 < \sigma_3$) and substituted into Equation B-15 to yield the individual strain rate components; viz,

$$\begin{aligned}\dot{\epsilon}_{11}^{\omega_s} &= \dot{\epsilon}_{22}^{\omega_s} = \dot{\epsilon}_{eq}^{\omega_s} \left(\frac{2\kappa}{\sqrt{3}} - \frac{3+\kappa}{12} \right) \\ \dot{\epsilon}_{33}^{\omega_s} &= \dot{\epsilon}_{eq}^{\omega_s} \left(\frac{2\kappa}{\sqrt{3}} + \frac{3+\kappa}{6} \right) \\ \dot{\epsilon}_v^{\omega_s} &= 2\sqrt{3} \kappa \dot{\epsilon}_{eq}^{\omega_s}\end{aligned}\tag{B-20}$$

Thus material parameter κ is seen to govern the magnitude of the volumetric strain generated during the microfracturing process associated with damage.

B.3 REFERENCES

Callahan, G. D., 1982. *A Plasticity Approach for Rock Containing Planes of Weakness*, Ph.D. Thesis, University of Minnesota, Minneapolis, MN.

Chen, W. F. and D. J. Han, 1988. *Plasticity for Structural Engineers*, Springer-Verlag, New York, NY.

Nayak, G. C. and O. C. Zienkiewicz, 1972. "A Convenient Form of Invariants and its Application in Plasticity," *Journal of the Structural Division*, ASCE, Vol. 98, pp. 949–954.